Draft version June 10, 2026
Typeset using LaTeX **twocolumn** style in AASTeX7.0.1

Through the Veil: Lyα Illuminates the Host Galaxies of Little Red Dots

Zhiyuan Ji [1], Yang Sun [1], Mauro Giavalisco [2], Anna de Graaff [3,4,*], Christina C. Williams [5,1], Yongda Zhu [1], George H. Rieke [1], and Marcia Rieke [1]

[1] *Steward Observatory, University of Arizona, 933 N. Cherry Avenue, Tucson, AZ 85721, USA*
[2] *University of Massachusetts Amherst, 710 North Pleasant Street, Amherst, MA 01003-9305, USA*
[3] *Center for Astrophysics, Harvard & Smithsonian, 60 Garden St, Cambridge, MA 02138, USA*
[4] *Max-Planck-Institut für Astronomie, Königstuhl 17, D-69117 Heidelberg, Germany*
[5] *NSF–DOE Vera C. Rubin Observatory/NSF NOIRLab, 950 N. Cherry Ave., Tucson, AZ 85719, USA*

ABSTRACT

Little Red Dots (LRDs) are enigmatic, compact red sources ubiquitous in JWST deep fields whose physical nature remains elusive. As one of the most sensitive tracers of neutral hydrogen in galaxy environments, Lyα is uniquely positioned to probe the gaseous structures proposed to explain LRDs' unusual properties. We present a systematic study of Lyα emission in LRDs, using a sample of 110 spectroscopically confirmed LRDs at $z \geq 4$ from the A. de Graaff et al. (2025a) catalog, all with NIRSpec/PRISM coverage of the Lyα line. We detect Lyα at signal-to-noise S/N ≥ 3 in 32 LRDs, finding Lyα luminosities and the distribution of rest-frame equivalent widths consistent with normal star-forming galaxies at comparable redshifts. Yet the Lyα/Hα ratios fall systematically below those of star-forming galaxies, and the Lyα luminosity tracks [O III] luminosity more closely than [O III] equivalent width, together suggesting that Lyα is primarily associated with the host-scale component rather than the compact component responsible for the broad Balmer lines and red continuum. For 13 LRDs at $z \gtrsim 5.5$, we construct continuum-subtracted Lyα maps using broadband imaging from HST/ACS or JWST/NIRCam, revealing spatially extended, asymmetric, and often offset emission relative to the rest-optical light, consistent with resonant scattering through clumpy, anisotropic gas commonly observed in high-redshift Lyα emitters. These results support a two-component picture in which the compact rest-optical source is embedded within a more extended host-galaxy environment whose interstellar and circumgalactic gas shapes Lyα escape and spatial redistribution. Lyα opens a new window into the relation between the compact red component, the host galaxy, and the surrounding gas in LRDs.

1. INTRODUCTION

The *James Webb Space Telescope* (JWST) has uncovered a remarkable population of compact, red sources at high redshift, commonly referred to as little red dots (LRDs; e.g., J. Matthee et al. 2024). These systems occupy a region of parameter space not well represented by previously known galaxy or quasar populations, exhibiting V-shaped spectral energy distributions from rest-frame UV to near-infrared (NIR), extremely compact rest-frame optical/NIR morphologies, and, in many cases, broad Balmer emission lines (e.g., J. E. Greene et al. 2024; R. E. Hviding et al. 2025). This unusual combination of properties, together with their apparently high abundance at $z \gtrsim 4$, has made LRDs central to current debates on the emergence of early black holes and the nature of luminous compact red sources in the first ∼1–2 Gyr of cosmic history.

A central question is what powers LRDs and whether they represent a single physical class. One widely discussed interpretation is that many LRDs host obscured active galactic nuclei (AGN), motivated by their compact morphologies, broad Balmer lines, and luminous red optical continua (J. Matthee et al. 2024; J. E. Greene et al. 2024; D. D. Kocevski et al. 2025; A. J. Taylor et al. 2025; I. Labbe et al. 2025). At the same time, alternative interpretations have invoked massive post-starburst or dusty star-forming galaxies; and the weak X-ray emission, low dust masses, and lack of strong hot-dust signatures suggest that LRDs are not simply scaled-down analogs of ordinary unobscured quasars (I. Labbé et al. 2023; P. G. Pérez-González et al. 2024; T. T. Ananna

Corresponding author: Zhiyuan Ji
zhiyuanji@arizona.edu

* Clay Fellow

et al. 2024; M. Yue et al. 2024; C. C. Williams et al. 2024; B. Wang et al. 2025; D. J. Setton et al. 2025; C. M. Casey et al. 2025; M. Xiao et al. 2025).

More recent work has proposed a picture in which at least some LRDs are powered by accreting black holes embedded in dense gaseous environments, where the observed continuum and line emission are strongly shaped by reprocessing in the surrounding medium (K. Inayoshi & R. Maiolino 2025; X. Ji et al. 2025; R. P. Naidu et al. 2025; A. de Graaff et al. 2025b; V. Rusakov et al. 2026; S.-J. Chang et al. 2026). This interpretation is supported by A. de Graaff et al. (2025a), who argue from a large spectroscopic sample that many LRD continua are well described by modified blackbodies, and that the optical continuum, Hα, Hβ, and O I emission are tightly linked, while [O III] is more naturally associated with the host galaxy.

The picture of a dense nuclear medium is also consistent with the idea that Balmer-line widths need not be purely virial, but may be shaped in part by scattering in dense gas, with important implications for inferred black-hole masses and growth rates (V. Rusakov et al. 2026; S.-J. Chang et al. 2026; R. P. Naidu et al. 2025; A. Torralba et al. 2026a; J. E. Greene et al. 2026). This possibility is additionally supported by the observations from A. Torralba et al. (2026b) and P. G. Pérez-González et al. (2026), who find that the Fe II/Mg II ratios of LRDs imply Eddington ratios of ~ 0.5. When combined with the bolometric luminosities of the nuclear sources, these Eddington ratios yield black-hole masses that are lower by orders of magnitude than estimates based purely on the Balmer-line widths. More broadly, several theoretical studies have connected such dense envelopes to quasistar-, black-hole-star-, or super-Eddington-accretion-like scenarios, in which high gas columns can naturally explain the red optical continua, strong Balmer features, and X-ray weakness of many LRDs (M. C. Begelman et al. 2008; F. Pacucci & R. Narayan 2024; K. Inayoshi & K. Ichikawa 2024; E. Lambrides et al. 2024; M. C. Begelman & J. Dexter 2026a; D. Kido et al. 2025; H. Liu et al. 2025; S. Zhang et al. 2026). Establishing how these different components are spatially related is therefore central to understanding the LRD phenomenon.

A key empirical insight from recent studies is that the rest-frame UV and optical emission in LRDs likely trace primarily different components. Spectral decompositions of large LRD samples indicate that the central engine contributes a median of $\sim$20% to the rest-UV continuum of a typical LRD, with the remainder arising from the host (W. Q. Sun et al. 2026). Yet identifying the dominant ionizing source from rest-UV emission lines alone has proven challenging, both because single-component AGN or stellar models cannot simultaneously reproduce the UV continuum, Balmer break, and broad lines of individual LRDs (Y. Ma et al. 2025), and because the relevant UV emission-line diagnostics suffer from well-known degeneracies between AGN- and star-formation-driven ionization at high redshift (e.g., H. Treiber et al. 2025). On the imaging side, while the redder light is frequently extremely compact, the UV can be extended, asymmetric, and/or multi-component (e.g., M. Killi et al. 2024; D. D. Kocevski et al. 2025; P. Rinaldi et al. 2025; E. Iani et al. 2025; A. P. Cloonan et al. 2026), independently suggesting that the UV emission often arises at least partly in the putative host galaxy rather than in the compact source that dominates the optical continuum. At the same time, however, UV morphology alone cannot determine how the ionizing source is embedded within, or obscured by, the surrounding neutral gas.

In this context, Lyα offers a uniquely powerful probe of the gaseous environment around LRDs. Because Lyα is resonantly scattered, its strength, line profile, and spatial distribution are highly sensitive to the neutral-gas column density, covering fraction, kinematics, dust content, and the topology of escape channels (e.g., M. Dijkstra 2014; M. Hayes 2015). Recent ultra-deep UV spectroscopy of the prototypical LRD Abell2744-QSO1 at $z = 7.04$, initially discovered by L. J. Furtak et al. (2023a), has already shown that the Lyα profile itself strongly constrains the gas geometry, disfavoring a uniform high-covering-fraction envelope and instead favoring a clumpy or porous medium with low-column-density escape channels (M. Tang et al. 2026; X. Ji et al. 2026). Whereas the Lyα spectral profile provides a global, galaxy-integrated view of how photons escape through the surrounding gas, its spatial distribution reveals where that escaping and scattered emission emerges. In particular, spatially resolved Lyα can distinguish whether the emission emerges directly from the nuclear region, diffuses through an extended scattering halo, or appears offset because it escapes anisotropically through the surrounding medium. So far, however, our knowledge of spatially resolved Lyα in LRDs remains very limited: in one case, the MUSE observation shows weak and modestly extended Lyα emission from an LRD at $z \sim 4.5$, favoring a highly enshrouded central source rather than a luminous quasar-like Lyα halo (A. Torralba et al. 2026b). Extending such analyses to larger samples is essential for understanding how Lyα properties connect to the nature of the LRD population.

In this paper, we investigate the Lyα properties of a large sample of spectroscopically confirmed LRDs from

A. de Graaff et al. (2025a); full details of the sample and associated data are provided in Section 2. We first characterize the integrated Lyα properties across the full sample at $z \geq 4$ (Section 3). While integral-field spectroscopy would offer the most direct probe of spatially resolved Lyα, such observations remain scarce for the high-redshift LRD population. We therefore leverage the wealth of existing broadband imaging from JWST/NIRCam and *Hubble Space Telescope* (HST) to construct continuum-subtracted Lyα maps for the subsample with robust Lyα detections at $z \gtrsim 5.5$ (Section 4). By comparing the integrated and spatially resolved views of Lyα with the rest-frame UV and optical continuum, we constrain the relation between the compact red component, the UV host emission, and the surrounding neutral gas, thereby clarifying which physical components are traced by Lyα in LRDs (Section 5).

Throughout this work, we adopt the AB magnitude system and the ΛCDM cosmology with Planck Collaboration et al. (2020) parameters, i.e., $\Omega_m = 0.315$ and $h = H_0/(100\,\mathrm{km\,s^{-1}\,Mpc^{-1}}) = 0.673$.

2. THE SAMPLE AND DATA

Our parent sample is drawn from A. de Graaff et al. (2025a)[6], who used the DAWN JWST Archive (DJA) to construct a uniformly selected sample of 146 LRDs at $z = 2.0$–9.3. Their selection requires both a V-shaped UV–optical continuum in the NIRSpec/PRISM spectra and a compact morphology in NIRCam/F444W imaging, yielding an intentionally conservative, high-purity sample with a remarkably high broad-Balmer-line detection rate of 98%. A. de Graaff et al. (2025a) show that these objects form a coherent spectroscopic family that is likely distinct from ordinary obscured Type 1 AGNs. This makes their sample a large, high-confidence set of classical LRDs well suited for population studies. The major surveys included in this LRD selection are CANUCS (G. T. E. Sarrouh et al. 2026), CAPERS (M. Dickinson et al. 2024), CEERS (S. L. Finkelstein et al. 2025), JADES (D. J. Eisenstein et al. 2026), MoM (R. P. Naidu et al. 2026), NEXUS (Y. Shen et al. 2024), NIRSpec GTO-Wide (M. V. Maseda et al. 2024), RUBIES (A. deGraaff et al. 2025), and UNCOVER (R. Bezanson et al. 2024). Additional programs were also considered; we refer readers to A. de Graaff et al. (2025a, and references therein) for further details.

In this work, we restrict our analysis to $z \geq 4$, where Lyα is covered by the nominal wavelength range of NIRSpec/PRISM (0.6–5.3 μm). Excluding 3 sources lacking usable Lyα coverage because the corresponding spectral region is affected by detector gaps or masking during data reduction, we have a final sample of 110 LRDs. Figure 1 shows the redshift distribution of the sample. We note that Abell2744-QSO1 (24175 in Figure 1) is multiply imaged by strong gravitational lensing, and its Lyα fluxes are fully consistent across the images within uncertainties (see Appendix A), so we include only one image of this source in Figure 1.

We use the NIRSpec/PRISM spectroscopic data from the DJA. Specifically, we adopt the public DJA NIRSpec reduction products from version 4.4 (K. E. Heintz et al. 2025; A. deGraaff et al. 2025). This latest version improves on the previous one by applying an empirical wavelength calibration correction based on the source centroid in the shutter, updating the flux-calibration reference files to extend the usable spectral range, and using optimal 1D extraction (K. Horne 1986) with a wavelength-dependent slit-loss correction.

For the spatially resolved Lyα analysis, we use the corresponding HST/ACS and NIRCam imaging data from the DJA reductions (F. Valentino et al. 2023). We adopt the latest DJA imaging release, version 7, for all fields containing LRDs, including GOODS-S (DJA imaging prefix: `gds`), Abell 2744 (`abell2744clu`), EGS (`ceers-full`), UDS (`primer-uds`), and COSMOS (`primer-cosmos`). The HST and NIRCam/LW images are all on 0.04″ pixel grids, while the NIRCam/SW data also have 0.04″ pixels in most fields, except in Abell 2744 and GOODS-S, where the mosaics are provided on 0.02″ pixel grids. All mosaics are astrometrically registered to a common world coordinate system (WCS) tied to Gaia DR3 (Gaia Collaboration et al. 2021).

3. INTEGRATED LY-ALPHA EMISSION IN LRDS

In this section, we investigate the integrated Lyα emission properties of the LRD sample using the JWST/NIRSpec PRISM spectra ($R \sim 100$). We first measure the Lyα line properties from the PRISM data through forward modeling of the continuum and line emission. We then compare the Lyα measurements with the UV-continuum, Balmer-line, and [O III] properties of the sources. These comparisons allow us to assess how Lyα emission relates to the UV and optical nebular properties of LRDs, and thereby provide insight into the physical origin and nature of Lyα emission in this population.

3.1. *Analysis*

We measure Lyα fluxes from the PRISM spectra by fitting the rest-frame spectral region blueward of 2500 Å. For each source, we model the intrinsic spectrum as the sum of a power-law continuum and a single Gaussian

[6] https://doi.org/10.5281/zenodo.17665942

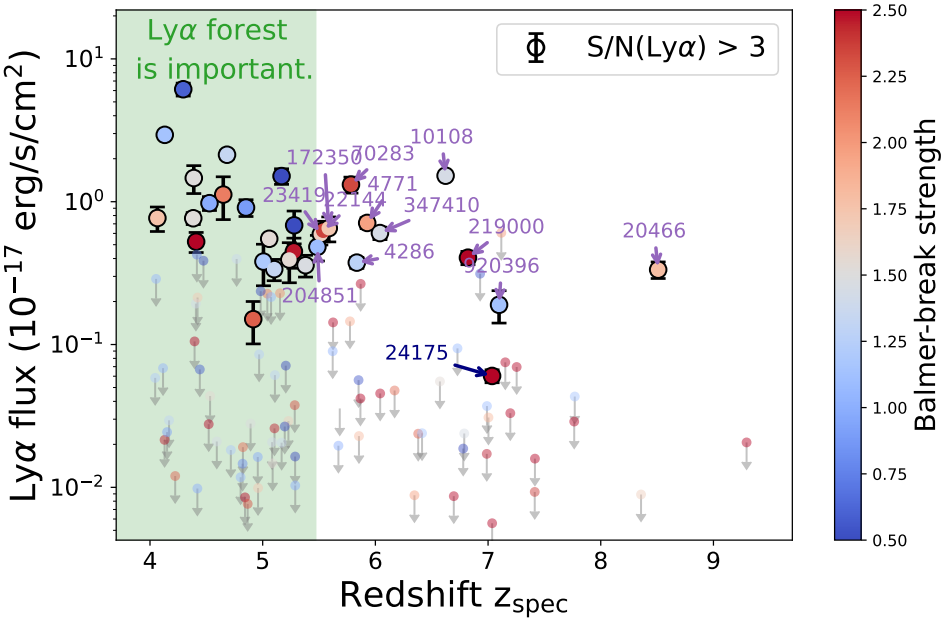

Figure 1. The final sample of 110 LRDs at $z \geq 4$ with NIRSpec/PRISM coverage of Lyα. Sources with Lyα detections at S/N ≥ 3 (see Section 3.1) are shown as circles with error bars, while the remaining sources are shown as upper limits on the Lyα flux. Sources are color-coded according to their Balmer-break strengths reported in A. de Graaff et al. (2025a). The LRDs at $z \geq 5.5$ labeled by their source IDs in this plot are those included in our spatially resolved Lyα analysis using broadband imaging (Section 4).

component representing Lyα,

$$f_\lambda^{\rm int}(\lambda) = A\left(\frac{\lambda}{\lambda_0}\right)^\beta + \frac{F_{\rm Ly\alpha}}{\sqrt{2\pi}\sigma_\lambda}\exp\left[-\frac{(\lambda-\lambda_{\rm Ly\alpha})^2}{2\sigma_\lambda^2}\right], \quad (1)$$

where A is the continuum normalization, β is the continuum slope, λ_0 is an arbitrary reference wavelength, $F_{\rm Ly\alpha}$ is the integrated Lyα flux and σ_λ is the Gaussian width. β is constrained by the continuum over the wavelength range 1300–2500 Å (D. Calzetti et al. 1994). Given the spectral resolution of the PRISM data, we fix $\lambda_{\rm Ly\alpha}$ based on the source redshift and use a Gaussian component as a simple empirical description of the Lyα emission profile.

To account for absorption by the Intergalactic Medium (IGM), we multiply the intrinsic model by the IGM transmission curve appropriate for the source redshift following A. K. Inoue et al. (2014). The transmitted model spectrum is therefore

$$f_\lambda^{\rm trans}(\lambda) = f_\lambda^{\rm int}(\lambda)\, T_{\rm IGM}(\lambda, z), \quad (2)$$

where $T_{\rm IGM}(\lambda, z)$ is the IGM transmission function. Because the observed spectra are additionally broadened by the instrumental response, we convolve the transmitted model with the wavelength-dependent NIRSpec/PRISM line-spread function (LSF)[7],

$$f_\lambda^{\rm model}(\lambda) = f_\lambda^{\rm trans}(\lambda) \otimes {\rm LSF}_{\rm PRISM}(\lambda). \quad (3)$$

We determine the best-fit parameters using a Markov Chain Monte Carlo (MCMC) analysis with the package EMCEE (D. Foreman-Mackey et al. 2013). The likelihood is constructed assuming Gaussian-distributed flux uncertainties,

$$\ln\mathcal{L} = -\frac{1}{2}\sum_i\left[\frac{\left(f_{\lambda,i}^{\rm obs} - f_{\lambda,i}^{\rm model}\right)^2}{\sigma_i^2} + \ln(2\pi\sigma_i^2)\right], \quad (4)$$

where $f_{\lambda,i}^{\rm obs}$ and σ_i are the observed flux density and its uncertainty in the ith spectral pixel, respectively. The free parameters in the fit are the continuum normalization, continuum slope, Lyα width, and Lyα flux. We adopt the posterior distribution from the MCMC chains to estimate the best-fit Lyα flux and its associated uncertainty. Throughout this work, we define a Lyα detection as a source with S/N $\equiv F_{\rm Ly\alpha}/\sigma(F_{\rm Ly\alpha}) \geq 3$. For sources with S/N < 3, we instead report the 1σ upper limit, $F_{\rm Ly\alpha}^{\rm UL}$, derived from the posterior distribution such

[7] https://jwst-docs.stsci.edu/jwst-near-infrared-spectrograph/nirspec-instrumentation/nirspec-dispersers-and-filters#gsc.tab=0

that $\int_0^{F_{\rm Ly\alpha}^{\rm UL}} P(F_{\rm Ly\alpha})\, dF_{\rm Ly\alpha} = 0.68$. In addition to the Ly$\alpha$ flux, the MCMC fitting also constrains the underlying UV continuum, from which we derive $M_{\rm UV}$ for each source. All fitting results of the Lyα-detected LRDs, including the best-fit parameters and data–model comparison plots, are presented in Appendix A.

In our fiducial Lyα modeling, we do not include a damped Lyα absorption (DLA) component, because DLA detectability is generally poor in PRISM $R \sim 100$ spectra (M. Huberty et al. 2025). However, we test the impact of this assumption in Appendix B by repeating the Lyα flux measurements with an additional DLA component. Based on the Bayesian information criterion (BIC), the vast majority of the LRD PRISM spectra do not show evidence for strong DLA absorption. Including the DLA component changes the measured Lyα fluxes by only $\sim 20\%$ and therefore does not affect any of the conclusions of this work.

Finally, to place the Lyα measurements in the broader context of the optical spectral properties of LRDs, we also make use of existing measurements of their rest-frame optical features. Specifically, in the subsequent analysis, we adopt Hα, the Balmer decrement, and [O III] measurements from A. de Graaff et al. (2025a). Because these measurements are based on NIRSpec/PRISM spectra, we use the total Hα luminosities rather than attempting a broad/narrow decomposition.

3.2. *Results*

3.2.1. *Lyα vs. UV continuum*

We first compare the integrated Lyα properties of the LRD sample with their UV continuum. The analysis proceeds in two complementary steps: (i) a comparison of the Lyα-detected LRDs to ordinary Lyα emitters (LAEs) in the $L_{\rm Ly\alpha}$–$M_{\rm UV}$ plane; and (ii) a comparison of the Lyα detection fraction, $X_{\rm Ly\alpha}$, against UV-selected Lyman-break galaxies for the full LRD sample. The two steps together cover the LRD populations with and without Lyα detections.

For the detected-vs-detected comparison, we use the LAEs of J. Kerutt et al. (2022) as a benchmark for ordinary high-redshift galaxies. By construction this LAE sample is restricted to Lyα-detected sources, containing ~ 2000 LAEs at $2.9 < z < 6.6$ with Lyα measurements from MUSE-Wide+Deep (R. Bacon et al. 2017; H. Inami et al. 2017; E. C. Herenz et al. 2017; T. Urrutia et al. 2019) and UV continuum constraints from archival HST imaging (M. Giavalisco et al. 2004; A. M. Koekemoer et al. 2011; N. A. Grogin et al. 2011). We focus on their subsample at $z \geq 4$.

As shown in the left panel of Figure 2, the Lyα-detected LRDs do not appear exceptional compared with the MUSE LAEs in the $L_{\rm Ly\alpha}$–$M_{\rm UV}$ plane: they overlap with the locus occupied by the LAEs with $-20 \lesssim M_{\rm UV} \lesssim -17$, with a p-value of ~ 0.2 from a two-dimensional K–S test (J. A. Peacock 1983; G. Fasano & A. Franceschini 1987). We emphasize that this statement applies to the Lyα-detected subsamples; whether the similarity extends to the full LRD population, which contains a substantial fraction of Lyα upper limits visible in Figure 2, is addressed separately by the $X_{\rm Ly\alpha}$ analysis later presented in this section.

We also examine the rest-frame Lyα equivalent-width distribution shown in Figure 3. We do not attempt to fit the intrinsic EW distribution of the LRD sample here, because such an analysis would require a careful treatment of completeness and selection effects. In particular, the LRD spectra used in this work are drawn from a heterogeneous set of surveys and programs, whose combined selection function is difficult to quantify in a uniform way. Nevertheless, it is notable that the observed EW distribution of the Lyα-detected LRDs is broadly consistent with that of normal LAEs at similar redshifts. Taken together, these indicate that, *when Lyα is detected*, the UV and Lyα properties of LRDs are not unusual compared with those of ordinary high-redshift star-forming galaxies.

To extend the comparison to the full LRD population regardless of Lyα detections, we turn to the Lyα detection fraction at fixed UV luminosity, $X_{\rm Ly\alpha}$, defined as the number of LRDs with Lyα detections divided by the total number of LRDs in a given $M_{\rm UV}$ bin. This second-tier comparison is benchmarked against UV-selected Lyman-break galaxies, which are not preselected on Lyα and therefore include both detections and non-detections.

The right panel of Figure 2 shows the $X_{\rm Ly\alpha}$ of the LRDs. For comparison, we show the measurements from D. P. Stark et al. (2010), based on Keck and VLT spectroscopy for Lyman-break galaxies over $3 < z < 7$, and from G. C. Jones et al. (2024), based on recent deep NIRSpec spectroscopy from the JADES program that provides updated constraints on the Lyα emitter fraction at $z \gtrsim 5$. Many other studies have reached broadly similar conclusions for Lyman-break galaxies over this redshift range using a variety of surveys and spectroscopic data sets (e.g., Y. Ono et al. 2012; L. Pentericci et al. 2014, 2018). The measured $X_{\rm Ly\alpha}$ values for LRDs are broadly consistent with these previous measurements for Lyman-break galaxies at similar redshifts and UV luminosities. This suggests that, from the perspective of UV-selected Lyα visibility, LRDs do not appear to form a distinct Lyα population. Instead, their Lyα detection fraction appears broadly consistent with

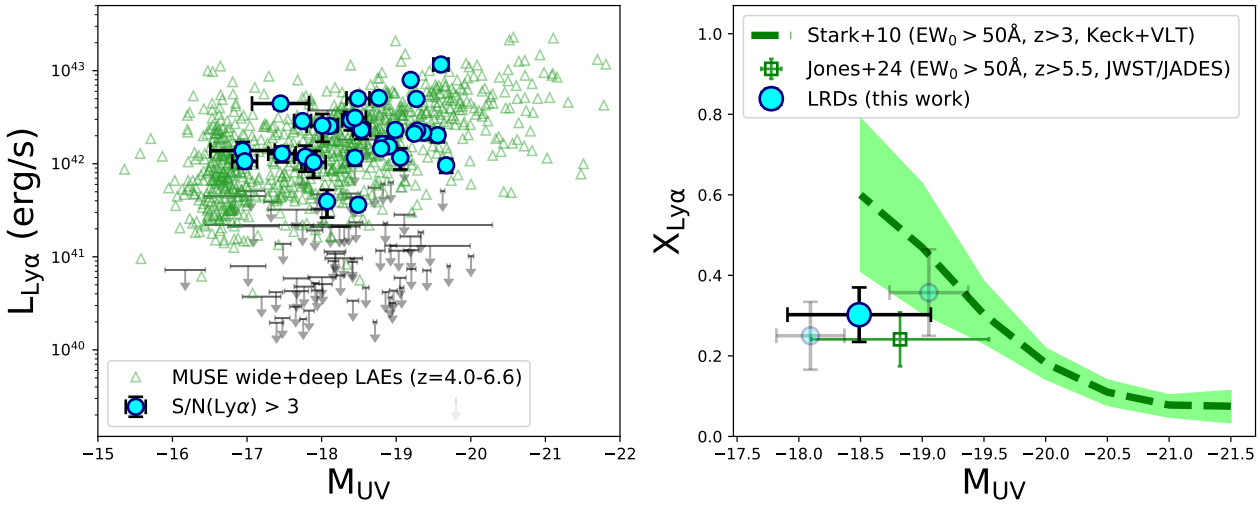

Figure 2. Left: Lyα luminosity as a function of UV absolute magnitude for the LRD sample. Sources with Lyα detections at S/N ≥ 3 are shown as circles with error bars, while non-detections are shown as upper limits. For comparison, the green triangles show MUSE-Wide+Deep Lyα emitters at $z = 4.0$–6.6 from J. Kerutt et al. (2022). **Right:** Lyα detection fraction, $X_{\mathrm{Ly}\alpha}$, as a function of M_{UV} for the full LRD sample, shown by the cyan circle with a black edge. We also divide the LRD sample into two subsamples using the median M_{UV}, shown by the light-cyan circles with gray edges. For comparison, we show measurements for Lyman-break galaxies from D. P. Stark et al. (2010) and G. C. Jones et al. (2024) with rest-frame EW$_0$ > 50 Å, broadly matching the observed Lyα equivalent widths of our Lyα-detected LRDs (see Figure 3).

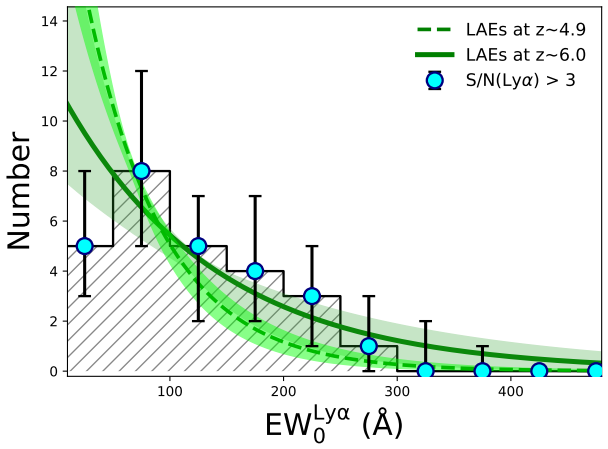

Figure 3. Rest-frame Lyα equivalent-width ($\mathrm{EW}^0_{\mathrm{Ly}\alpha}$) distribution. The blue circles with error bars show the Lyα-detected LRDs in our sample. The uncertainties are estimated by bootstrapping the sample and resampling each EW measurement using its corresponding fitting uncertainty derived in Section 3.1. For comparison, the green shaded histograms and curves show the $\mathrm{EW}^0_{\mathrm{Ly}\alpha}$ distributions of MUSE Hubble Ultra Deep Field LAEs at $z \sim 4.9$ and $z \sim 6.0$ from T. Hashimoto et al. (2017).

that of the broader high-redshift galaxy population, although a fully homogeneous comparison would require a detailed treatment of the heterogeneous selection functions and spectroscopic depths.

3.2.2. *Lyα vs. Balmer lines*

We next compare the integrated Lyα emission of LRDs with their Balmer-line properties in Figure 4. As a benchmark for normal high-redshift star-forming galaxies, we use the sample of X. Lin et al. (2024), which combines Hα measurements from NIRCam/WFSS spectroscopy acquired by the FRESCO program (P. A. Oesch et al. 2023) with Lyα measurements from MUSE for star-forming galaxies at $z = 4.9$–6.3 (R. Bacon et al. 2017, 2023). In the left panel of Figure 4, we compare $L_{\mathrm{Ly}\alpha}$ and $L_{\mathrm{H}\alpha}$, and also show the expected relation from Case B recombination for different levels of dust attenuation. Relative to both these expectations and the X. Lin et al. (2024) comparison sample, the LRDs lie systematically low in Lyα at fixed Hα. In other words, although many LRDs have luminous Balmer emission, their escaping Lyα is faint compared with that of ordinary star-forming galaxies with similar Hα luminosities. This indicates that the Balmer emission in LRDs is not accompanied by proportionally strong Lyα, in contrast to what would be expected if both lines traced the same gas under ordinary nebular conditions.

We further compare $L_{\mathrm{Ly}\alpha}/L_{\mathrm{H}\alpha}$ with $L_{\mathrm{H}\alpha}/L_{\mathrm{H}\beta}$ in the right panel of Figure 4. Because X. Lin et al. (2024) do not have Hβ measurements for their sample, we estimate $L_{\mathrm{H}\alpha}/L_{\mathrm{H}\beta}$ from their SED-based dust attenuation using the D. Calzetti et al. (2000) attenuation law. In this panel, we also show the expected relation from Case B recombination for different Lyα escape fractions. Nor-

mal galaxies from the X. Lin et al. (2024) sample broadly follow the expected trend in which dust attenuation and varying Lyα escape fraction move galaxies through this plane. By contrast, the LRDs occupy a clearly different region, with relatively low Lyα/Hα yet large Hα/Hβ. We also show the typical line ratios of Type I quasars (D. E. Vanden Berk et al. 2001) and $z \gtrsim 6$ red quasars (Y. Matsuoka et al. 2025), shown as orange and purple hexagons, respectively. The observed hydrogen line ratios in LRDs are likewise distinct from those of quasars.

Taken together, these results indicate that the Lyα and Balmer emission in LRDs are not simply scaled versions of the nebular emission seen in ordinary galaxies, but instead point to a different effective line-emitting and/or Lyα-escaping environment. As discussed in Section 3.2.1, the escaping Lyα is consistent with being dominated by host-galaxy star formation. If so, the Lyα-emitting gas should also produce Hα and Hβ, but with a Balmer ratio characteristic of normal H II regions rather than that of the dominant LRD component.

This picture makes a testable spatial prediction. If the Lyα-emitting gas is distributed differently from the compact central engine, as suggested by the spatially resolved analysis in Section 4, then the Balmer decrement should vary with position in LRDs where Lyα is detected. To test this, we stack the 2D NIRSpec/PRISM spectra of the Lyα-detected and Lyα-undetected subsamples separately and measure Hα/Hβ as a function of spatial position, restricting the analysis to $4 \leq z \leq 7$, where Hα falls within the PRISM range. For each source we subtract a per-row linear continuum fitted to the rest-frame sidebands of each line, resample onto a common rest-frame grid, and normalize by the continuum at rest-frame 5100 Å before stacking into mean, median, and inverse-variance-weighted (IVW) 2D spectra. For each spatial row we then measure Hα by integrating over 6400–6750 Å (wide enough to enclose both the narrow and broad components) and Hβ over 4800–4925 Å, after removing the per-row best-fit [O III]$\lambda\lambda$4959, 5007 Gaussians with the doublet ratio fixed at 2.98 (P. J. Storey & C. J. Zeippen 2000). Gaussian fitting yields ratios consistent with this box integration to within $\sim$ 5%, and uncertainties are derived from a bootstrap-plus-Monte Carlo procedure (200 resamplings per subsample, each spectrum perturbed by its error map before re-stacking and re-fitting).

Figure 5 shows the resulting Hα/Hβ as a function of position. While the absolute decrement depends on the stacking weights, the trends are qualitatively consistent across the three stacks. The Lyα-undetected stack shows no clear spatial variation, remaining consistent with a constant decrement across the inner $\pm 0.2''$. The Lyα-detected stack, however, shows evidence that Hα/Hβ decreases from the trace center toward off-trace positions.

This off-trace trend must be interpreted with care. At the sample median $z \approx 5$, the observed Hα and Hβ fall at ≈ 4 and ≈ 3 μm, where the NIRSpec/PRISM cross-dispersion PSF FWHM ($\approx 0.2''$) is comparable to the outermost bin in which the decrement is still measurable, so the off-trace spectra remain significantly contaminated by the central source through the PSF wings. Even so, the fact that Hα/Hβ declines with offset in the Lyα-detected stack but not in the Lyα-undetected one suggests that, when Lyα is detectable, an additional emission component contributes that is both more spatially extended and has a lower Balmer ratio than the dominant central component. Together with Figure 4, these measurements suggest that the dominant Balmer-line emission and the escaping Lyα are not tracing the same gas under ordinary nebular conditions.

3.2.3. *Lyα vs. [O III]λ5007 emission*

In Figure 6 we compare the integrated Lyα emission of LRDs with their [O III] properties. In the left panel we plot $L_{\mathrm{Ly}\alpha}$ against $L_{[\mathrm{O\,III}]}$ and compare the LRDs with the $z \sim 5$–6 galaxy sample of S. Hashemi et al. (2025). The LRDs broadly overlap with the locus occupied by these normal high-redshift galaxies, suggesting that, at fixed [O III] luminosity, the escaping Lyα emission in LRDs is consistent with that of the broader galaxy population.

We quantify the trends in Figure 6 using the Spearman rank correlation coefficient, r_s. We estimate the uncertainty in r_s with a bootstrap procedure, in which we resample the Lyα-detected sources and perturb their measurements according to the observational uncertainties. The Lyα luminosity is correlated with $L_{[\mathrm{O\,III}]}$, with $r_s = 0.30 \pm 0.05$. Its correlation with $\mathrm{EW}_{[\mathrm{O\,III}]}$ is weaker, with $r_s = 0.18 \pm 0.05$, and is driven almost entirely by a single source with $\mathrm{EW}_{[\mathrm{O\,III}]} > 2000$ Å; removing this object reduces the coefficient to $r_s < 0.1$ ($p > 0.9$), consistent with no correlation. We further assess whether the difference between the two correlation strengths is meaningful by computing $\Delta r_s = r_s(L_{\mathrm{Ly}\alpha}, L_{[\mathrm{O\,III}]}) - r_s(L_{\mathrm{Ly}\alpha}, \mathrm{EW}_{[\mathrm{O\,III}]})$ within each bootstrap realization. Among the 10^4 bootstrap realizations, $\approx 95\%$ yield $\Delta r_s > 0$, suggesting, at modest significance, that the luminosity–luminosity relation is stronger than the relation with equivalent width.

Although the modest size of the Lyα-detected LRD sample means that larger samples will be needed to confirm it, this difference in correlation strength is already physically suggestive. If the rest-frame optical contin-

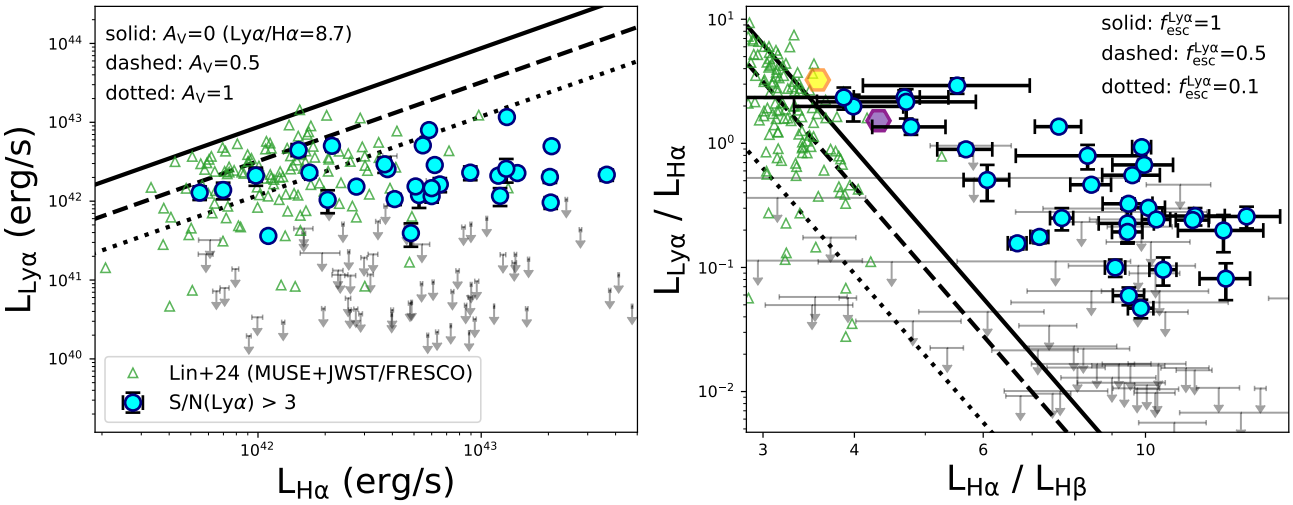

Figure 4. Left: Lyα luminosity as a function of Hα luminosity for the LRD sample. Sources with Lyα detections at S/N ≥ 3 are shown as circles with error bars, while non-detections are shown as upper limits. The green triangles show the comparison sample of normal star-forming galaxies from X. Lin et al. (2024). The black curves show the expected relation assuming Case B recombination with $n_e = 10^2$ cm^{-3} and $T_e = 10^4$ K (D. E. Osterbrock & G. J. Ferland 2006), attenuated with the D. Calzetti et al. (2000) dust law for $A_V = 0$, 0.5, and 1.0 mag. **Right:** $L_{Ly\alpha}/L_{H\alpha}$ as a function of $L_{H\alpha}/L_{H\beta}$ for the same samples. The black curves are constructed by assuming the Case B recombination and adopting different Lyα escape fractions, $f_{esc}^{Ly\alpha} = 1$, 0.5, and 0.1. The orange hexagon marks the line ratios of the SDSS Type I quasar composite (D. E. Vanden Berk et al. 2001). The purple hexagon marks the median line ratios of the $z \gtrsim 6$ red quasars from the SHELLQs survey (Y. Matsuoka et al. 2025).

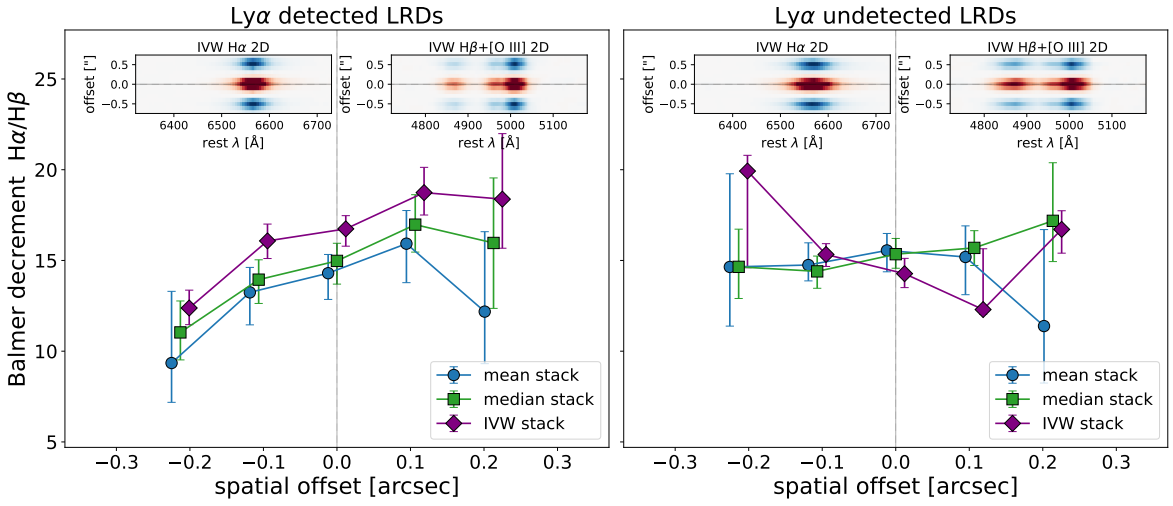

Figure 5. Balmer decrement, Hα/Hβ, as a function of spatial position for the Lyα-detected (left) and Lyα-undetected (right) LRD subsamples, measured from stacked 2D NIRSpec/PRISM spectra. Results from three different stacking weights are shown: mean (blue circles), median (green squares), and inverse-variance-weighted (IVW; purple diamonds). Error bars are estimated from bootstrap resamplings, as described in Section 3.2.2. The insets at the top of each panel show the IVW Hα 2D stack and the IVW Hβ+[O III] 2D stack.

uum near [O III] arose from the same physical component as the [O III]-emitting gas, then normalizing the line luminosity by that continuum, i.e. using $\mathrm{EW}_{[\mathrm{O\,III}]}$ rather than $L_{[\mathrm{O\,III}]}$, should not substantially weaken its correlation with Lyα. Instead, we observe the opposite: the luminosity–luminosity relation is stronger, suggesting that the optical continuum introduces additional scatter that is less closely linked to the gas regulating Lyα escape. This interpretation is consistent with recent work arguing that the red optical continuum in LRDs is closely tied to the compact central component, whereas [O III] emission arises predominantly in the host galaxy (e.g., A. de Graaff et al. 2025a; W. Q. Sun et al. 2026). If Lyα likewise traces gas on host-galaxy scales, as suggested by the preceding sections, then a tighter relation with $L_{[\mathrm{O\,III}]}$ than with $\mathrm{EW}_{[\mathrm{O\,III}]}$ follows naturally: the continuum entering the equivalent-width denominator originates, at least in part, from a distinct physical component. Our results therefore provide supporting evidence for a picture in which the optical continuum and the [O III]-emitting gas are at least partly associated with distinct physical components in LRDs.

4. SPATIALLY RESOLVED LY-ALPHA EMISSION IN LRDS AT $Z \geq 5.5$

The HST and NIRCam imaging provide a powerful way to constrain the two-dimensional Lyα emission in LRDs at sub-kpc resolution by combining a Lyα-sensitive broadband filter with adjacent continuum filters. Such an analysis, however, requires a statistically robust treatment of IGM transmission. At lower redshifts, the Lyα forest transmission affects the flux blueward of Lyα, introducing redshift-dependent and sightline-dependent contamination into broadband Lyα measurements (e.g., G. D. Becker et al. 2015; S. E. I. Bosman et al. 2018; A.-C. Eilers et al. 2018). Once the Gunn–Peterson trough (J. E. Gunn & B. A. Peterson 1965) becomes effective, the IGM is essentially opaque blueward of Lyα, allowing the broadband flux to be more cleanly separated into Lyα emission and redward UV continuum. We therefore restrict this analysis to $z \gtrsim 5.5$. This redshift cut is intentionally conservative relative to the nominal transition at $z \approx 5.3$, often associated with the end of reionization (e.g., Y. Zhu et al. 2021; S. E. I. Bosman et al. 2022), because even modest residual uncertainties in IGM transmission can bias spatially resolved Lyα maps more severely than integrated flux measurements.

There are a total of 47 galaxies at $z \gtrsim 5.5$ in the A. de Graaff et al. (2025a) sample with usable NIRSpec/PRISM Lyα coverage. Of these, 13 show Lyα emission detected at S/N ≥ 3 in NIRSpec and have the required HST and/or NIRCam Lyα imaging coverage. These 13 LRDs are the focus of the subsequent spatially resolved Lyα analysis. Their detailed information can be found in Table 1.

4.1. *Analysis*

To produce the spatially resolved Lyα maps, we first identify, for each source, the broadband filter that contains redshifted Lyα and a set of adjacent redward UV filters, covering rest-frame $\approx 1500-3000$ Å, that can be used to constrain the underlying continuum (Table 1).

We then homogenize the imaging to a common PSF. In most legacy fields, we use the NIRCam empirical point spread functions (ePSFs) released by the DJA (A. Genin et al. 2025)[8]. Abell 2744 is treated separately because the DJA does not provide NIRCam PSFs for that field. Although the UNCOVER team provides PSFs for Abell 2744 (J. R. Weaver et al. 2024), these are defined on a $0\farcs04$ pixel grid, whereas we retain the native DJA $0\farcs02$ pixel scale for the NIRCam/SW mosaics in order to preserve the best possible spatial information. We therefore construct our own NIRCam/SW ePSFs for Abell 2744 following J. Anderson & I. R. King (2000), and verify that they are highly consistent with the UNCOVER ePSFs (see Appendix C). Similarly, we construct ePSFs for the HST/ACS bands relevant to this study. We then compute the PSF-matching kernels using PYPHER (Boucaud, A. et al. 2016) and convolve all relevant images to match the broadest PSF among the filters used for that source (see Table 1).

After PSF matching, we predict the UV continuum contribution in the Lyα band on a pixel-by-pixel basis. We model the UV continuum as a power law, $f_\lambda = A\lambda^\beta$, and compute the expected continuum flux in the Lyα-sensitive filter by integrating this spectrum through the filter transmission curve, $R(\lambda)$, while also including the wavelength-dependent IGM transmission, T_{IGM}, at the source redshift:

$$f_{\mathrm{cont}} = \frac{\int A\lambda^\beta\, T_{\mathrm{IGM}}(z,\lambda)\, R(\lambda)\, \lambda\, d\lambda}{\int R(\lambda)\, \lambda\, d\lambda}. \tag{5}$$

For the IGM model, we adopt that of A. K. Inoue et al. (2014). We have verified that our results do not change if we instead use the P. Madau (1995) model. We consider two approaches for the continuum modeling. In our fiducial method, we allow β to vary from pixel to pixel and determine the best-fitting value directly from the imaging, thereby accounting for possible spatial variations in the UV continuum slope across the source. As

[8] https://dawn-cph.github.io/dja/blog/2024/08/16/morphological-data/

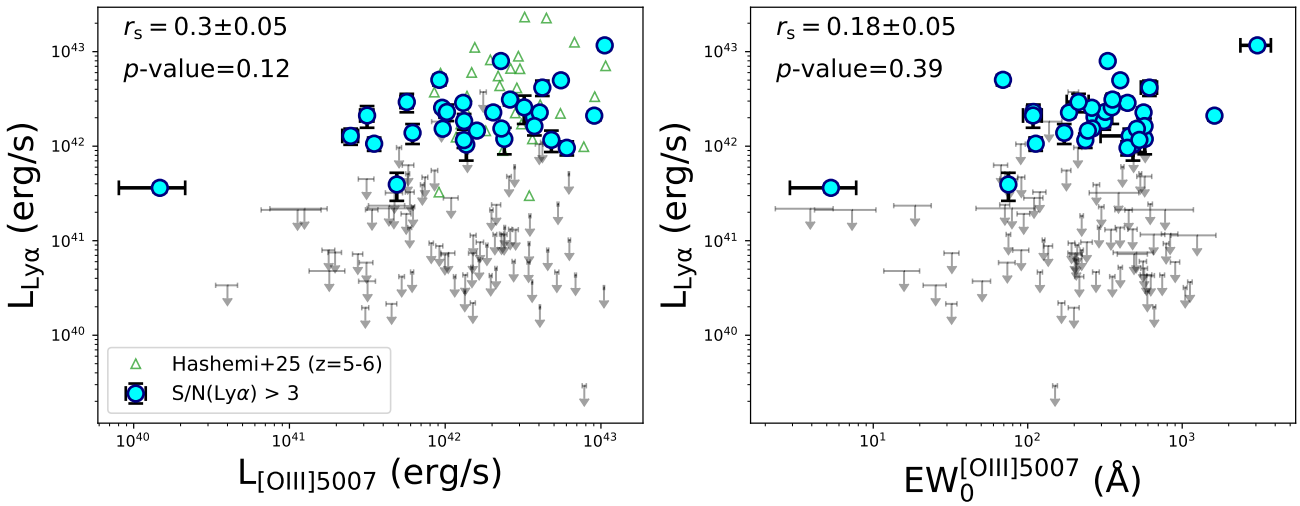

Figure 6. Left: Lyα luminosity as a function of [O III]λ5007 luminosity. The green triangles show the comparison sample of normal $z \sim 5$–6 galaxies from S. Hashemi et al. (2025). **Right**: Lyα luminosity as a function of rest-frame [O III]λ5007 equivalent width. In each panel, the quoted Spearman rank correlation coefficient r_s is estimated from bootstrap resampling; the quoted uncertainty corresponds to the dispersion of the resulting r_s distribution.

Table 1. Lyα-detected LRD sample at $z \geq 5.5$ for the spatially resolved analysis

Source ID	Field	z_{spec}	$F_{Ly\alpha,DJA}$ (10^{-18} erg/s/cm^2)	S/N$_{Ly\alpha}$	Lyα Filter	UV Continuum Filter
204851	GOODS-S	5.49	4.83	4.9	HST/F775W	(F850LP†, F090W, F115W, F150W)
23419	UDS	5.52	5.93	6.2	HST/F814W†	(F090W, F115W, F150W)
22144	COSMOS	5.54	6.27	6.1	HST/F814W†	(F090W, F115W, F150W)
172350	UDS	5.59	6.53	5.0	F090W	(F115W, F150W, F200W†)
70283	COSMOS	5.78	13.20	7.8	F090W	(F115W, F150W, F200W†)
4286	A2744	5.84	6.02	11.3	F090W	(F115W, F150W, F200W†)
4771	COSMOS	5.93	7.10	11.3	F090W	(F115W, F150W, F200W†)
347410	COSMOS	6.04	6.03	10.0	F090W	(F115W, F150W, F200W†)
10108	EGS	6.62	15.21	26.9	F090W	(F115W, F150W, F200W†)
219000	GOODS-S	6.82	4.06	9.3	F090W	(F115W, F150W, F200W†)
24175	A2744	7.04	4.14	9.6	F090W	(F115W, F150W, F200W†)
920396	UDS	7.10	1.90	3.9	F090W	(F115W, F150W, F200W†)
20466	A2744	8.51	4.51	7.5	F115W	(F150W, F200W†)

† The filter to which all other filters are PSF-matched.

NOTE—Columns: (1) source ID in A. de Graaff et al. (2025a); (2) survey field; (3) spectroscopic redshift; (4) apparent DJA spectroscopic Lyα flux; (5) DJA Lyα signal-to-noise ratio; (6) broadband filter containing Lyα, with HST filters indicated; and (7) broadband filters used to derive the continuum at the Lyα wavelength.

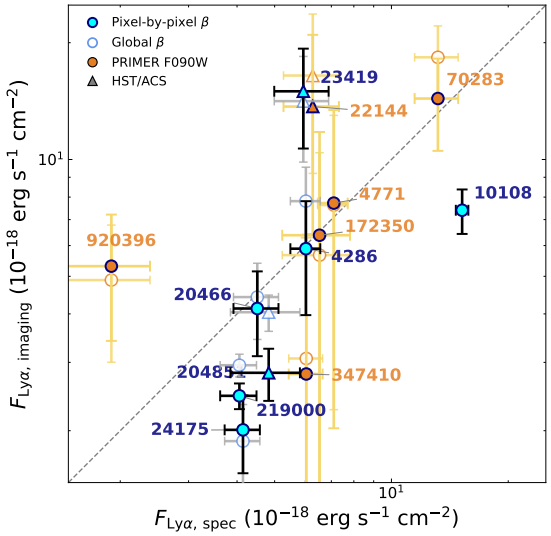

Figure 7. Comparison of Lyα fluxes measured from spectroscopy (x-axis) and from our broadband imaging continuum-subtraction method (y-axis), where the latter are computed by summing the Lyα maps within a circular aperture of radius $r = 0\farcs16$ centered on the F444W centroid. Filled symbols show the results obtained with pixel-by-pixel UV β fitting, while open symbols show those obtained using a global β. Circles denote Lyα measurements derived from NIRCam imaging, while triangles denote those derived from HST/ACS imaging. The dashed line marks the 1:1 relation.

a consistency check, we also perform an alternative fit in which β is fixed to the global UV slope inferred from the integrated photometry and only the normalization is solved for in each pixel. These two methods provide complementary estimates of the continuum and allow us to assess the robustness of the inferred Lyα morphology.

With the PSF-matched imaging and the predicted UV continuum map at the Lyα wavelength in hand, we construct the Lyα map by subtracting the continuum image from the observed image of the Lyα-sensitive band. We then convert the residual broadband excess into a Lyα line-flux map. In practice, we note that noise and continuum-model uncertainties can lead to formally negative Lyα fluxes in some pixels, which do not represent physically meaningful emission. We therefore define the displayed Lyα map as $\max(F_{\mathrm{Ly}\alpha}, 0)$ on a pixel-by-pixel basis, while retaining the full signed residuals for uncertainty estimation and other quantitative checks.

The spatially resolved Lyα maps presented in this work rely on accurate WCS alignment across different filters. As described in Appendix D, we perform a detailed astrometric analysis for each source and find that the relative WCS alignment reaches sub-pixel precision in all cases, sufficient for the subsequent analysis of the Lyα spatial distribution.

We note that the fidelity of the resulting Lyα maps depends on the depth of the Lyα-sensitive band, which varies across fields. For the majority of the sources, Lyα falls in F090W, and the PRIMER COSMOS and UDS F090W mosaics are appreciably shallower than those in the other fields. The Lyα maps for sources in these two fields are therefore noticeably noisier, and we present them separately in Appendix E.

Finally, in Figure 7, we compare the Lyα fluxes derived from NIRSpec spectroscopy with those measured from our Lyα maps. We find overall good agreement within the uncertainties. This consistency is seen for both the pixel-by-pixel β fitting and the global β fitting methods, demonstrating that our results are not highly sensitive to the specific treatment of the UV continuum slope. Consistent with the depth differences noted above, the COSMOS and UDS sources (orange symbols in Figure 7), whose Lyα-sensitive imaging is drawn from the shallower PRIMER mosaics, exhibit significantly larger uncertainties than the sources in the deeper fields.

4.2. *Results*

Figures 8 and 9 present the spatially resolved Lyα maps for the LRDs at $z \gtrsim 5.5$ in Abell 2744, GOODS-S, and EGS; the maps for the COSMOS and UDS sources are shown in Appendix E.

In the resolved maps, the Lyα-sensitive image shows a clear flux excess over the predicted continuum, and in many cases the inferred Lyα emission is not centered exactly on the compact rest-optical component. Instead, across most of the sample, the inferred Lyα morphology is asymmetric, patchy, and/or displaced relative to the F444W centroid. In some objects, the emission is clearly offset from the compact F444W centroid (24175, 20466, 10108 and 219000), while in others it is distributed in an irregular or clumpy pattern around the rest-optical centroid (4286 and 204851). A particularly remarkable case is the GOODS-S source 204851 (Figure 9), which, in addition to a diffuse component, exhibits two distinct clump-like structures in the Lyα-sensitive imaging rather than a single centrally concentrated component. The lower/southern clump is independently confirmed to belong to the same system and also shows strong Lyα emission (see Appendix F), demonstrating that escaping Lyα can be associated with a spatially complex, multi-component structure rather than being confined to the compact F444W core. A more detailed study of this source will be presented by Z. Ji et al. (2026, in prep.).

The Lyα emission also appears to be more extended than the adjacent UV continuum. We explore this dif-

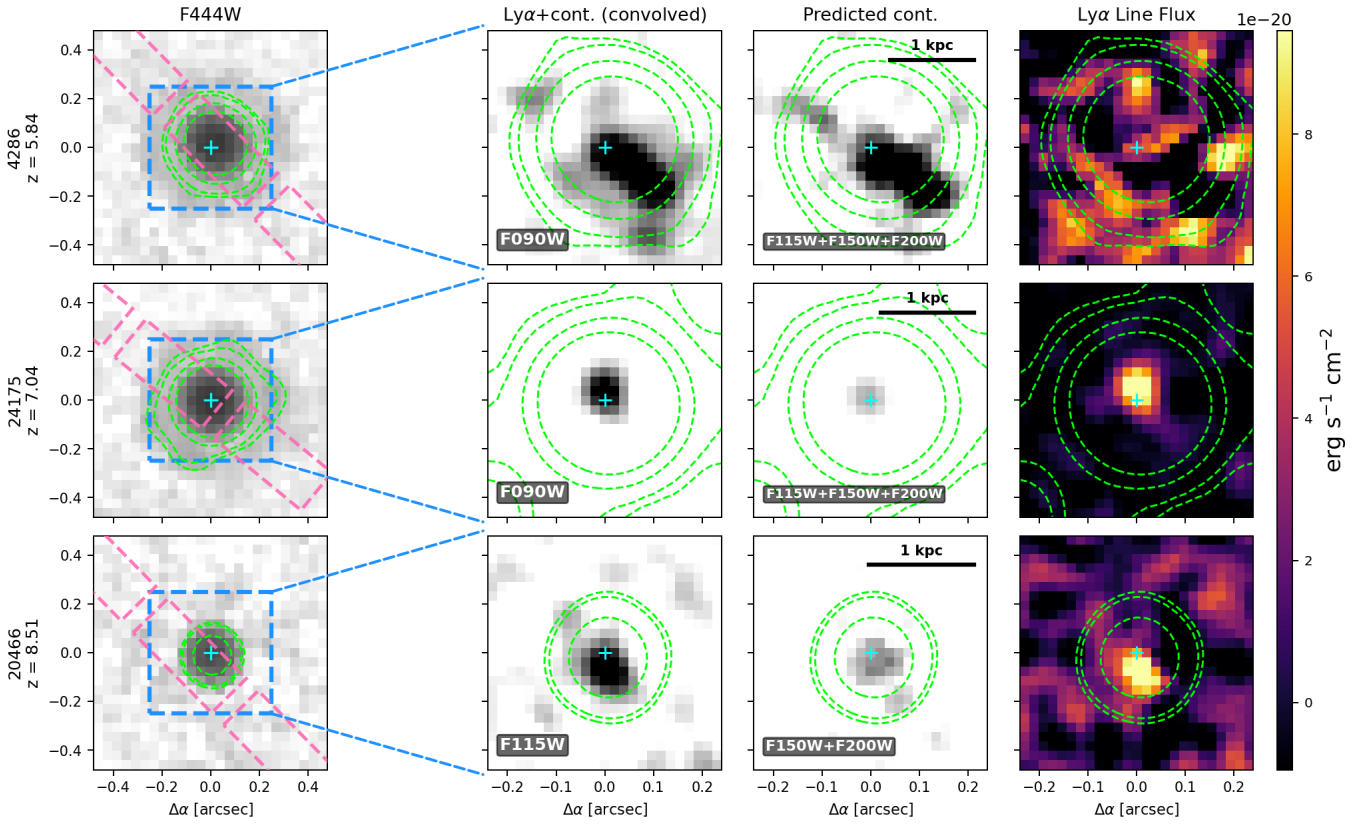

Figure 8. Spatially resolved Lyα maps for three LRDs in Abell 2744. The sources are identified by the IDs shown on the far left. For each source (row), the panels show: (1) the NIRCam/F444W image displayed with a logarithmic color scale, with the MSA slit overplotted in dark pink; (2) the PSF-matched broadband image containing Lyα + continuum; (3) the predicted UV continuum in the Lyα filter from the pixel-by-pixel β fit; and (4) the continuum-subtracted Lyα line-flux map. Green dashed contours show the F444W surface brightness at 4σ, 5σ, 10σ, and 20σ, while cyan crosses mark the F444W centroid determined using `photutils.centroids`. The Lyα-filter and continuum panels are PSF-matched and share a common grayscale; therefore, a darker appearance in the Lyα + continuum image than in the continuum-only image implies a flux excess due to Lyα. Filter names are annotated in the lower-left corner of each panel.

ference by performing single-Sérsic fitting with GALFIT (C. Y. Peng et al. 2010). We restrict this morphological analysis to the non-PRIMER sources, as the shallower COSMOS and UDS images (Section 4.1) do not yield reliable size measurements. Because the continuum-subtracted Lyα maps do not have sufficient S/N for a meaningful morphological analysis, we compare the morphology measured from the Lyα-sensitive image, which contains Lyα+continuum, with that measured from the adjacent continuum-only image. All GALFIT analyses presented here were performed on the corresponding images at their nominal resolutions. Given the generally faint UV emission of the LRDs, we perform two sets of fits: one with the Sérsic index n fixed at 1 (i.e., an exponential disk) and one with n left free. As shown in Figure 10, the Lyα-sensitive image is typically more extended than the adjacent continuum-only images. We note that this result does not provide a direct measurement of the Lyα effective radius, but it is consistent with an additional Lyα component contributing at larger radii than the UV continuum.

Such offset, asymmetric, and spatially extended Lyα morphologies are not unique to LRDs. Similar phenomenology is commonly observed in ordinary high-redshift Lyα emitters and in local compact starbursts, where resonant scattering redistributes Lyα photons into a more extended and irregular component than the stellar UV light (e.g., M. Hayes et al. 2005; H. Atek et al. 2008; G. Östlin et al. 2009; C. C. Steidel et al. 2011; L. Wisotzki et al. 2016; F. Leclercq et al. 2017). These studies show that extended Lyα halos and spatial offsets between Lyα and the stellar continuum are common outcomes of radiative transfer through an inhomogeneous neutral medium rather than signatures unique to any one galaxy class. Therefore, at least at the phenomenological level, the Lyα morphologies of LRDs seem to be broadly consistent with this picture.

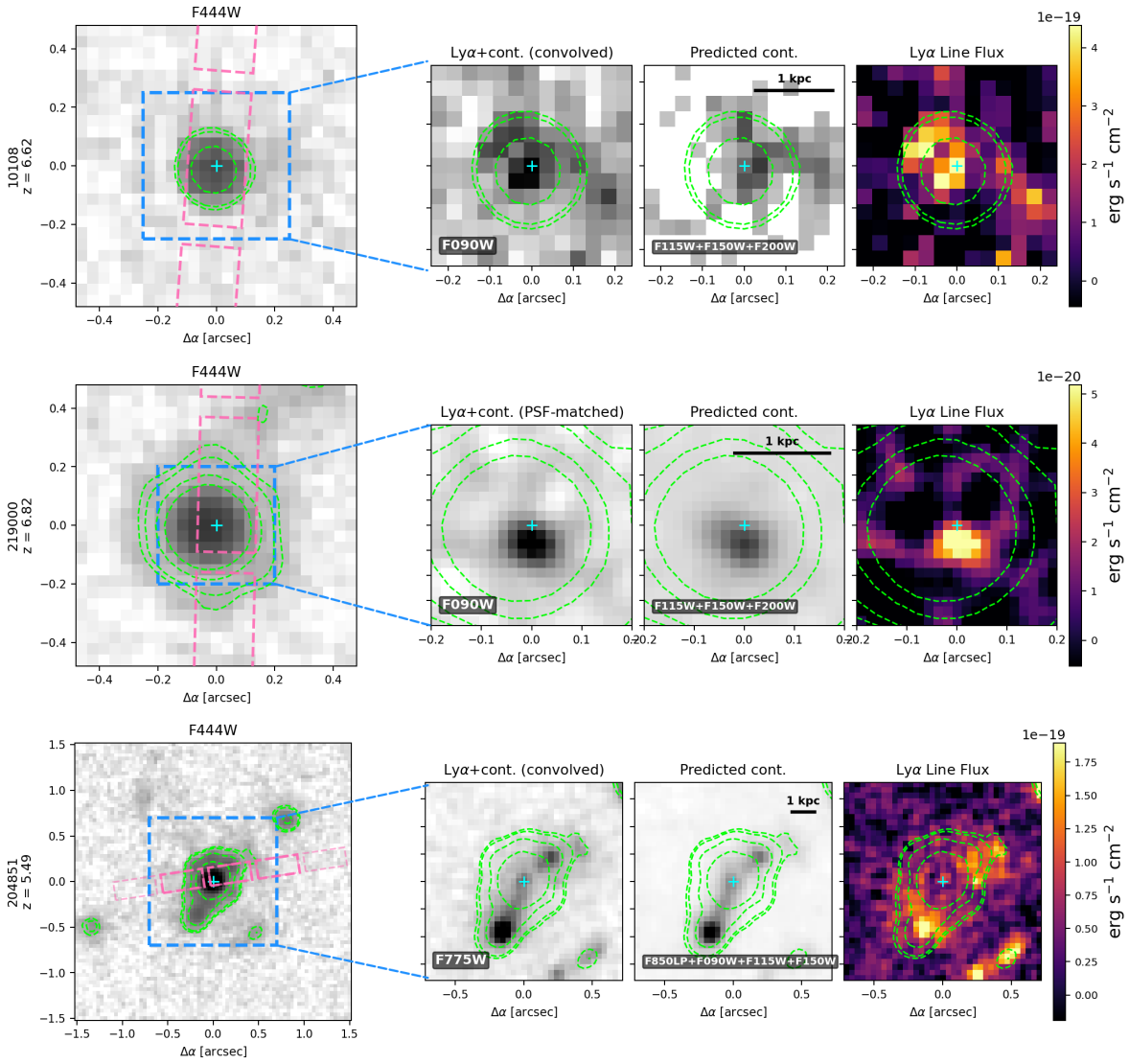

Figure 9. Similar to Figure 8, but for the LRDs in EGS (first row) and GOODS-S (second and third rows).

5. DISCUSSION

5.1. *The origin of Lyα in LRDs*

From the perspective of integrated Lyα properties alone, LRDs are not obviously distinguishable from the broader population of star-forming galaxies at similar redshifts. Their Lyα luminosities, UV–Lyα relations, and rest-frame equivalent-width distributions are all broadly consistent with those of ordinary high-redshift galaxies of comparable UV brightness (Section 3.2.1). Phenomenologically, therefore, the Lyα emission emerging from LRDs appears fairly typical.

What makes LRDs distinctive is the contrast between these ordinary Lyα properties and their extraordinary optical spectra. Relative to their strong Balmer emission, the escaping Lyα is systematically weak: the LRDs in our sample are offset toward low $L_{\mathrm{Ly}\alpha}/L_{\mathrm{H}\alpha}$ compared to star-forming galaxies at similar redshifts (Section 3.2.2). Meanwhile, the Lyα luminosity correlates more closely with $L_{[\mathrm{O\,III}]}$ than with [O III] EW (Section 3.2.3), and the spatially resolved maps show Lyα morphologies that are extended, asymmetric, patchy, and frequently offset from the compact rest-optical component traced by F444W (Section 4). Taken together, these results suggest that the observed Lyα does not primarily trace the compact component that dominates the red optical continuum and broad Balmer lines, but instead behaves as a tracer of gas on host-galaxy scales.

This connection is consistent with the emerging picture from optical spectroscopy. A. de Graaff et al. (2025a) and W. Q. Sun et al. (2026) argue that [O III] is more naturally associated with the host galaxy than with the compact component that produces the red continuum and broad Balmer lines, and Y. Pang et al.

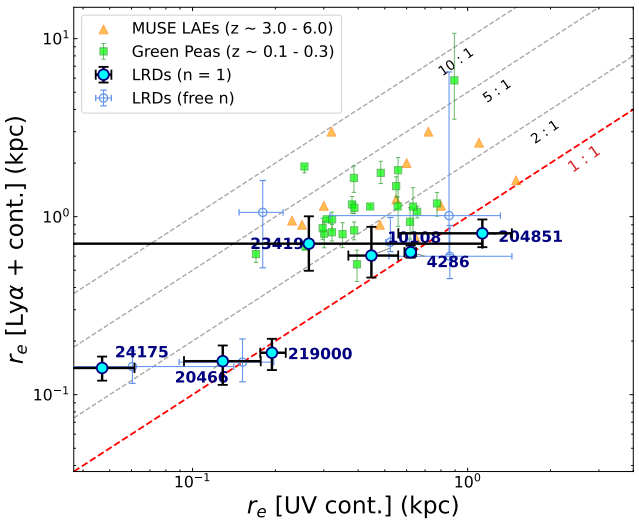

Figure 10. Effective radius measured from the Lyα-sensitive image (y-axis) versus that measured from the adjacent UV-continuum image (x-axis) for the $z \geq 5.5$ LRDs. Orange and green points show comparison samples of MUSE LAEs at $z \sim 3$–6 and Green Peas at $z \sim 0.1$–0.3, respectively, measured by H. Yang et al. (2017). We note that these comparison-sample measurements trace the Lyα size directly, as they are derived from either MUSE IFU or HST/COS 2D spectroscopy, whereas our measurements are based on the Lyα-sensitive broadband image and therefore correspond to Lyα+continuum. Error bars (1σ) are estimated from resampling of the image pixel values using the sigma maps, followed by 100 repeated `galfit` fits. Only the non-PRIMER sources are shown, because the shallower COSMOS and UDS images do not yield reliable size measurements.

(2026) find that [O III] correlates with the UV continuum rather than with the optical. The UV continuum itself is increasingly attributed to young stellar populations in the host galaxy (Y. Asada et al. 2026; M. Killi et al. 2024; P. Rinaldi et al. 2025), although the contribution from the central component may still be non-negligible (W. Q. Sun et al. 2026; M. Ando et al. 2026). The fact that Lyα tracks [O III] and shares qualitatively similar spatial characteristics with the UV emission is consistent with Lyα being primarily associated with the same host-scale component.

A natural question is why Lyα associated with the compact and much brighter (relative to UV) rest-optical component, if produced there at all, does not dominate the observed emission. In the dense-envelope framework, several factors may contribute. A growing body of theoretical work has shown that the red optical continuum, strong Balmer breaks, and broad Balmer lines of LRDs can be reproduced by models in which an accreting black hole is embedded in a dense gaseous cocoon, whether framed as a dense neutral gas envelope (K. Inayoshi & R. Maiolino 2025; X. Ji et al. 2025), a "black hole star" atmosphere (R. P. Naidu et al. 2025; D. Kido et al. 2025), a dense ionized cocoon with electron-scattering line broadening (V. Rusakov et al. 2026; S.-J. Chang et al. 2026), a late-stage quasi-star (F. Pacucci & R. Narayan 2024; M. C. Begelman & J. Dexter 2026b), or an orientation-dependent super-Eddington accretion flow (P. Madau & R. Maiolino 2026). A common feature of these models is that the compact component is surrounded by gas of high column density, which has direct implications for Lyα. Self-consistent radiative-transfer calculations predict that the inner ionized region is bounded by a cold gas reservoir with neutral column densities $N_{\rm HI} \sim 10^{23}$ cm^{-2}, sufficient to produce strong Lyα absorption, and that little UV flux is transmitted directly from the accretion region (A. Sneppen et al. 2026). In a complementary analysis, Y. Asada et al. (2026) argue that both the UV continuum and much of the Hα emission in LRDs are powered by young massive stars surrounding the envelope rather than by the AGN itself, and find that Lyα occurrence rates in LRDs are comparable to those in ordinary star-forming galaxies, which is consistent with Lyα originating in, or being reprocessed through, host-scale gas associated with the extended stellar component rather than in the cocoon.

A further possible connection between Lyα and the dense-envelope picture emerges from the anomalous Balmer decrements observed in many LRDs (Figure 4). At the gas densities inferred for the cocoon ($n_{\rm H} \sim 10^{9\text{–}11}$ cm^{-3}), collisional excitation populates the hydrogen $n = 2$ level to the point where the gas becomes optically thick to the Balmer transitions themselves (K. Inayoshi & R. Maiolino 2025; X. Ji et al. 2025). In this regime, Hβ photons resonantly scatter off $n = 2$ hydrogen and can convert to Paα + Hα via the $n = 4 \rightarrow 3$ cascade, systematically destroying Hβ and enhancing Hα (S.-J. Chang et al. 2026; R. P. Naidu et al. 2025). This process steepens the observed Balmer decrement well beyond the Case B value (Figure 4) and beyond what dust reddening alone can account for (G. P. Nikopoulos et al. 2025). Our stacking analysis of 2D spectra (Figure 5) offers additional, though currently tentative observational support for this association: among the Lyα-detected LRDs, the Balmer decrement is steepest at the position of the compact rest-optical source and appears to decline toward larger spatial offsets, as expected if the anomalous decrement originates in the dense central component while the more extended host gas approaches a more nearly Case B ratio. The same dense medium that drives this anomalous decrement would, by extension, be even more opaque to Lyα: if the $n = 2$ popula-

tion is sufficient to make Hα a resonant line, the $n = 1$ population would imply that any Lyα produced within or passing through the cocoon experiences extreme optical depths. The steep Balmer decrements and the weakness of Lyα from the compact component are therefore not independent observations but rather two manifestations of the same underlying condition: a dense gaseous envelope in which hydrogen radiative transfer departs strongly from the optically thin (Case B) limit.

The current data cannot uniquely determine whether the compact component fails to produce significant Lyα, produces it but the surrounding neutral gas absorbs it before escape, or contributes only a subdominant fraction that is overwhelmed by host-galaxy emission. What they do strongly suggest is that the observed Lyα behaves as a host-galaxy tracer. The complex, extended morphologies seen in our maps are the expected signatures of resonant scattering through a clumpy, anisotropic interstellar and circumgalactic medium (e.g., P. Laursen et al. 2009; Z. Zheng et al. 2010; M. Gronke et al. 2017), and are commonly observed in ordinary high-redshift Lyα emitters and local compact starbursts (e.g., M. Hayes et al. 2013; F. Leclercq et al. 2017). Detailed Lyα-profile studies of individual LRDs likewise favor porous or non-uniform gas geometries rather than fully closed configurations (M. Tang et al. 2026; X. Ji et al. 2026).

The picture that emerges is one in which the observed Lyα in LRDs is governed by the structure and geometry of gas on host-galaxy scales, aligning it with the UV continuum and [O III] rather than with the red optical continuum and broad Balmer lines. This reinforces the broader empirical picture in which the properties of LRDs reflect at least two spatially and physically distinct components: a compact inner region that dominates the red continuum and Balmer emission, and a host-galaxy environment traced by the UV, [O III], and now Lyα.

5.2. *Implications for the physical diversity of LRDs*

Whether LRDs constitute a single physical class remains an open question, and the answer depends sensitively, even primarily, on how the sample is defined. Photometric selections based on V-shaped continua, spectroscopic selections requiring broad Balmer lines, and morphological selections based on compactness in the rest-frame optical all yield overlapping but distinct samples with different levels of contamination and completeness (e.g., P. G. Pérez-González et al. 2026; P. Rinaldi et al. 2026). Studies that adopt broader photometric criteria tend to find a continuous distribution of properties with no sharp boundary separating LRDs from the general galaxy population (P. Rinaldi et al. 2026), while spectroscopically confirmed samples with strict broad-line and continuum-shape requirements isolate a more homogeneous subset (A. de Graaff et al. 2025a; B. Wang et al. 2025). Much of the apparent tension in the literature over whether LRDs are a distinct class likely reflects these differences in sample definition rather than a genuine disagreement in the underlying physics.

In this work, our sample is drawn from the spectroscopic catalog of A. de Graaff et al. (2025a), i.e. a sample that is by construction more uniform in its compact-component properties than purely photometric selections (Section 2). Our Lyα results therefore pertain specifically to this broad-line, V-shaped continuum, and compact population.

Within this sample, our central finding is that the observed Lyα more likely traces host-galaxy gas rather than the compact component. Because Lyα is governed by a different set of physical conditions (e.g., ISM covering fraction, dust/gas geometry, and star-formation activity) than those that define the LRD selection (continuum shape and compact morphology), the Lyα properties provide an additional degree of freedom that is largely independent of the compact-component diagnostics. The $\approx$30% Lyα detection rate, the scatter in Lyα luminosity at fixed Hα or [O III] luminosity, and the diversity of Lyα morphologies across our spatially resolved subsample likely reflect variations in host-galaxy environment rather than variations in the central engine or cocoon.

This interpretation naturally accommodates diversity even within a spectroscopically homogeneous LRD sample. Two LRDs with similar compact-component properties (e.g., comparable Balmer-break strength, optical luminosity) could exhibit very different Lyα properties if their host galaxies differ in ISM structure or star-formation activity. Conversely, the fact that LRD Lyα properties overlap broadly with those of ordinary star-forming galaxies suggests that the host-galaxy environments of these LRDs are not exceptional: it is the compact component that makes them unusual, not the galaxies in which they reside.

This two-component perspective, an unusual compact source embedded in a relatively ordinary host galaxy, offers a framework for understanding why even spectroscopically selected LRDs can appear diverse when examined across multiple diagnostics. Indicators sensitive to the compact component (broad Balmer lines, red continuum, Balmer break) track one axis of variation, while indicators sensitive to the host galaxy (UV morphology, [O III], and now Lyα) track another, likely independent axis. The observed scatter in LRD properties may

therefore reflect the natural variation expected when two physically distinct components – each with its own range of properties – contribute to the observed emission in different proportions. Future studies that jointly analyze Lyα, UV morphology, and optical spectral properties for larger samples will be able to test this picture by examining whether Lyα detection and morphology correlate with host-galaxy indicators (e.g., UV half-light radius, [O III] luminosity) independently of compact-component properties (e.g., Balmer-break strength, broad Hα luminosity).

6. CAVEATS

Our analysis relies on the spectroscopic catalog of A. de Graaff et al. (2025a), which selects LRDs based on V-shaped UV-to-optical continua and compact rest-optical morphology. These criteria yield a clean, spectroscopically coherent sample in which broad Balmer lines are found in ∼98% of cases, but prioritize purity over completeness, a trade-off that, in our view, is necessary when the physical nature of the population itself remains uncertain. This choice, however, necessarily excludes sources that may share similar physical origins but fall outside these strict criteria. R. E. Hviding et al. (2025) demonstrate that photometric and spectroscopic LRD selections overlap by only ∼50–60%, and broader photometric criteria reveal a continuous distribution of properties with no sharp boundary separating LRDs from the general galaxy population (e.g., P. Rinaldi et al. 2026; P. G. Pérez-González et al. 2026). The practical consequence is that our Lyα results, including detection rates, luminosity distributions, and spatial morphologies, may not be representative of the full population of objects commonly "labeled" as LRDs. Quantifying this effect is very challenging, if possible at all, given that no consensus yet exists on how to define an LRD selection that is simultaneously pure and complete. Our results thus apply specifically to the high-purity subsample identified by A. de Graaff et al. (2025a). Extending them to the broader LRD population will require Lyα analyses of complementary LRD samples selected using other criteria, together with a dedicated assessment of the systematics inherent to those selection methods.

7. SUMMARY

We have presented a systematic study of Lyα emission in Little Red Dots, using a sample of 110 spectroscopically confirmed LRDs at $z \geq 4$ drawn from the A. de Graaff et al. (2025a) catalog. All sources have NIRSpec/PRISM coverage of the Lyα line, and a subset of 13 at $z \gtrsim 5.5$ have the broadband imaging required for spatially resolved Lyα mapping.

We detect Lyα at S/N ≥ 3 in 32 LRDs, with $L_{\mathrm{Ly}\alpha}$ luminosities of $\sim 10^{41}$–10^{43} erg s^{-1}, rest-frame equivalent widths, and detection fractions all broadly consistent with those of ordinary star-forming galaxies at comparable redshifts and UV luminosities. From the perspective of their UV and Lyα properties alone, LRDs do not appear to form a distinct population. Yet what sets LRDs apart is the contrast between these ordinary Lyα properties and their extraordinary rest-optical spectra. The Lyα/Hα luminosity ratio is systematically lower than expected under Case B recombination, suggesting that the escaping Lyα emission is not simply proportional to the dominant Balmer-emitting component. Meanwhile, Lyα luminosity shows a stronger trend with [O III]λ5007 luminosity than with [O III] equivalent width. Although statistically modest, this behavior is consistent with Lyα being associated with host-scale gas rather than with the compact component that dominates the red continuum and broad Balmer lines.

The spatially resolved analysis reinforces this picture. Continuum-subtracted Lyα maps for 13 LRDs at $z \geq 5.5$ reveal extended, asymmetric, and often offset emission relative to the rest-optical light traced by F444W. GALFIT modeling of the Lyα-sensitive broadband images yields larger effective radii than adjacent continuum-only images, consistent with Lyα contributing on larger spatial scales than the adjacent UV continuum. These morphologies are consistent with resonant scattering through clumpy, anisotropic interstellar and circumgalactic gas, as commonly observed in high-redshift Lyα emitters and local compact starbursts.

Together, our integrated and spatially resolved measurements support a two-component picture of LRDs: a compact inner region that dominates the red optical continuum and broad Balmer emission, embedded within a more extended host-galaxy environment whose gas governs Lyα production and radiative transfer. Within this framework, the steep Balmer decrements and the weakness of Lyα from the compact component may be two manifestations of the same underlying condition: a dense gaseous envelope in which collisional excitation of hydrogen populates the $n = 2$ level, rendering both Balmer and Lyα photons susceptible to resonant scattering and destruction. The diversity of Lyα properties across the sample, spanning non-detections to luminous, spatially extended emission, more likely reflects variation in host-galaxy environments rather than in the compact component, establishing Lyα as a new and independent diagnostic for understanding the physical nature of LRDs.

ACKNOWLEDGMENTS

This work is based on observations made with the NASA/ESA/CSA James Webb Space Telescope. The data were obtained from the Mikulski Archive for Space Telescopes at the Space Telescope Science Institute, which is operated by the Association of Universities for Research in Astronomy, Inc., under NASA contract NAS 5-03127 for JWST. The spectroscopic observations are associated with programs 1180, 1181, 1208, 1212, 1213, 1215, 1286, 1345, 1433, 2198, 2561, 2750, 2767, 4106, 4233, 5105, 5224, 6368, 6541 and 6585. The imaging observations are associated with programs 1180, 1181, 1264, 1324, 1345, 1727, 1810, 1837, 1840, 1895, 1963, 2079, 2234, 2279, 2561, 2738, 2750, 2756, 3215, 3516, 3577, 4111, 4762, 6434, 6585.

ZJ, YS, YZ, GHR, and MR acknowledge support from the NIRCam Science Team contract to the University of Arizona, NAS5-02015. AdG acknowledges support from a Clay Fellowship awarded by the Smithsonian Astrophysical Observatory. The work of CCW is supported by NOIRLab, which is managed by the Association of Universities for Research in Astronomy (AURA) under a cooperative agreement with the National Science Foundation.

APPENDIX

A. UV CONTINUUM AND LYα SPECTRAL FITTING

Table 2 presents our spectral fitting results for all 32 LRDs at $z \geq 4$ from A. de Graaff et al. (2025a) that have Lyα detections with S/N ≥ 3. Figures 11, 12, and 13 show the individual spectral fits for the LRDs with S/N(Lyα) ≥ 3.

B. THE IMPACT OF DLA ON LYα MEASUREMENTS

In our fiducial analysis (Section 3.1) we do not include a DLA component, because the limited spectral resolution of the NIRSpec/PRISM data ($R \sim 100$) smears out the characteristic damping wings and makes a DLA difficult to detect and to disentangle from the IGM attenuation. To verify that this choice does not bias our measurements, here we repeat the fits with a DLA component included.

We model the DLA absorption following the same prescription as Z. Ji et al. (2025, their Section 5.2). The neutral hydrogen along the line of sight is treated as an ensemble of H I atoms, and the Lyα optical depth is computed by summing the corresponding Voigt profiles (J. S. Bolton & M. G. Haehnelt 2007). We fix the Doppler parameter to $b = 10$ km s^{-1}, a value commonly adopted in the literature, and place the absorbing gas at the systemic redshift of each source. Because this gas is local to the host galaxy, its transmission multiplies the intrinsic spectrum before IGM attenuation. We then refit every Lyα-detected LRD with this DLA-augmented model, retaining the same `emcee` set-up as in the fiducial analysis (Section 3.1). Because the DLA model includes one additional free parameter, we assess whether it is actually favored by the data using the Bayesian information criterion (BIC; G. Schwarz 1978), computing ΔBIC for each source.

Figure 14 compares the Lyα fluxes recovered with and without the DLA component. For the vast majority of the LRDs the DLA model is not preferred (ΔBIC < 5). The two sets of measurements track the 1:1 relation closely: including the DLA only fills in part of the absorbed line and continuum, so the fluxes are systematically equal to or slightly larger than the fiducial values, with a median change of just $\sim 20\%$. This is comparable to or smaller than the typical measurement uncertainties on $F_{\mathrm{Ly}\alpha}$. We therefore conclude that omitting a DLA component from our fiducial model introduces at most a $\sim 20\%$ systematic in the integrated Lyα fluxes and does not affect any of the conclusions of this work.

C. COMPARISON OF PSF MODELS

As mentioned in the main text (Section 4.1), to retain the finer pixel scale of the DJA mosaics in Abell 2744, we construct our own ePSFs for the four NIRCam/SW filters (F090W, F115W, F150W, and F200W) using isolated, unsaturated stars identified in the A2744 mosaic. The ePSFs are built at the native $0\farcs02$ pixel scale of the DJA mosaics using 22–27 stars per filter, following the iterative ePSF-fitting procedure of J. Anderson & I. R. King (2000), with a quartic oversampling kernel and careful sky subtraction around each stellar cutout.

Figure 15 compares our ePSFs with those provided by the UNCOVER team (J. R. Weaver et al. 2024) for all four filters. Overall, the two sets of profiles are highly consistent, agreeing to within $\sim 3-10\%$. A systematic trend is visible in the residuals at very small radii ($\lesssim 0.2''$), where our ePSFs exhibit slightly higher central surface

Table 2. UV spectral measurements of the LRDs with Lyα detections (S/N $\geq$ 3)

Source ID	PID	R.A. (deg)	Decl. (deg)	$z_{\rm spec}$	μ	$F_{\rm Ly\alpha}$ (10^{-18} erg s^{-1} cm^{-2})	EW$^0_{\rm Ly\alpha}$ (Å)	S/N	$\beta_{\rm UV}$	$M_{\rm UV}$ (mag)
20466	2561	3.6404084	-30.3864376	8.5095	1.35	$4.51^{+0.60}_{-0.59}$	$219.0^{+71.8}_{-52.3}$	7.5	$-1.52^{+0.48}_{-0.47}$	-18.45 ± 0.15
920396	5224	34.2478277	-5.1519963	7.0976	1.00	$1.90^{+0.49}_{-0.48}$	$38.8^{+11.2}_{-10.3}$	3.9	$-1.01^{+0.13}_{-0.13}$	-19.05 ± 0.04
15383[†]	2561	3.5835346	-30.3966786	7.0370	6.75	$5.75^{+0.32}_{-0.33}$	$89.7^{+6.5}_{-6.4}$	17.6	$-1.14^{+0.07}_{-0.07}$	-19.30 ± 0.02
24175[†]	2561	3.5798316	-30.4015692	7.0357	6.88	$4.14^{+0.44}_{-0.43}$	$130.6^{+21.9}_{-18.3}$	9.6	$-1.31^{+0.20}_{-0.20}$	-18.49 ± 0.06
16594[†]	2561	3.5972027	-30.3943287	7.0346	3.60	$1.70^{+0.34}_{-0.34}$	$106.7^{+29.2}_{-25.9}$	5.0	$-1.08^{+0.27}_{-0.27}$	-17.80 ± 0.08
219000	8060	53.1613700	-27.7376600	6.8215	1.00	$4.06^{+0.43}_{-0.44}$	$58.0^{+7.2}_{-6.8}$	9.3	$-1.29^{+0.09}_{-0.10}$	-19.28 ± 0.03
10108	6368	214.7975318	52.8187520	6.6231	1.00	$15.21^{+0.57}_{-0.56}$	$204.0^{+15.2}_{-14.2}$	26.9	$-1.65^{+0.12}_{-0.12}$	-19.19 ± 0.03
347410	5224	150.0729041	2.3236212	6.0405	1.00	$6.03^{+0.62}_{-0.59}$	$187.6^{+40.2}_{-32.0}$	10.0	$-1.38^{+0.33}_{-0.32}$	-18.11 ± 0.09
4771	6368	150.1610287	2.4658044	5.9273	1.00	$7.10^{+0.61}_{-0.64}$	$293.9^{+75.2}_{-58.2}$	11.3	$-1.40^{+0.40}_{-0.40}$	-17.74 ± 0.11
4286	2561	3.6192010	-30.4232703	5.8352	1.61	$6.02^{+0.54}_{-0.53}$	$94.2^{+12.2}_{-10.9}$	11.3	$-1.25^{+0.15}_{-0.15}$	-18.80 ± 0.04
70283	5545	150.0783330	2.3726864	5.7834	1.00	$13.18^{+1.68}_{-1.70}$	$271.0^{+107.9}_{-68.6}$	7.8	$-1.21^{+0.52}_{-0.49}$	-18.49 ± 0.15
172350	4233	34.3689512	-5.1039415	5.5865	1.00	$6.53^{+1.29}_{-1.30}$	$107.3^{+38.0}_{-29.9}$	5.0	$-1.67^{+0.45}_{-0.43}$	-18.53 ± 0.12
22144	5545	150.0637500	2.2467978	5.5370	1.00	$6.27^{+1.05}_{-1.00}$	$59.1^{+12.0}_{-10.6}$	6.1	$-0.61^{+0.13}_{-0.13}$	-19.36 ± 0.04
23419	6368	34.4711074	-5.1904554	5.5160	1.00	$5.93^{+0.96}_{-0.94}$	$37.2^{+7.0}_{-6.5}$	6.2	$-1.66^{+0.11}_{-0.11}$	-19.55 ± 0.03
204851	1286	53.1385932	-27.7902534	5.4855	1.00	$4.83^{+0.98}_{-0.98}$	$62.3^{+16.6}_{-14.4}$	4.9	$-1.38^{+0.22}_{-0.22}$	-18.82 ± 0.05
279078	5224	150.0828163	2.2777263	5.3801	1.00	$3.59^{+0.62}_{-0.63}$	$63.7^{+14.0}_{-13.1}$	5.8	$-1.29^{+0.20}_{-0.20}$	-18.45 ± 0.05
53692	4233	34.4553763	-5.2318140	5.2793	1.00	$6.84^{+1.75}_{-1.78}$	–	3.9	–	–
1020485	8018	189.1130858	62.2923908	5.2769	1.00	$4.49^{+1.04}_{-1.10}$	$245.0^{+332.7}_{-114.4}$	4.2	$-2.09^{+1.35}_{-1.40}$	-16.94 ± 0.43
12577	2198	53.0484548	-27.8151409	5.2363	1.00	$3.94^{+1.22}_{-1.24}$	$128.6^{+67.4}_{-48.8}$	3.2	$-0.96^{+0.50}_{-0.47}$	-17.78 ± 0.15
25191	5105	268.3795708	65.2023333	5.1674	1.00	$15.12^{+1.89}_{-1.88}$	$719.7^{+873.6}_{-291.9}$	8.0	$-0.56^{+1.06}_{-0.97}$	-17.45 ± 0.38
233464	5224	150.0716706	2.2004085	5.1024	1.00	$3.37^{+0.59}_{-0.55}$	$14.9^{+2.8}_{-2.6}$	5.9	$-1.96^{+0.06}_{-0.06}$	-19.67 ± 0.01
21547	2561	3.5508378	-30.4065978	5.0579	1.61	$8.86^{+0.45}_{-0.44}$	$91.1^{+6.7}_{-6.3}$	19.8	$-1.21^{+0.08}_{-0.08}$	-18.90 ± 0.02
3104035	1208	64.0562377	-24.1135383	5.0068	1.17	$4.45^{+1.46}_{-1.41}$	$105.6^{+67.6}_{-44.4}$	3.1	$-1.50^{+0.63}_{-0.61}$	-17.89 ± 0.16
312568	5224	150.1058493	2.4468234	4.9161	1.00	$1.51^{+0.47}_{-0.52}$	$34.0^{+12.2}_{-12.4}$	3.0	$-0.77^{+0.16}_{-0.15}$	-18.07 ± 0.05
39353	1181	189.2939522	62.1530911	4.8520	1.00	$9.10^{+1.21}_{-1.23}$	$63.7^{+11.5}_{-10.8}$	7.4	$-2.20^{+0.19}_{-0.18}$	-18.99 ± 0.05
4446	1215	34.2707118	-5.2176705	4.6835	1.00	$21.33^{+1.37}_{-1.35}$	$135.3^{+15.2}_{-12.7}$	15.6	$-1.03^{+0.14}_{-0.14}$	-19.27 ± 0.04
10835	5105	268.4376747	65.1674849	4.6501	1.00	$11.22^{+3.81}_{-3.64}$	$227.0^{+165.7}_{-96.1}$	3.0	$-0.89^{+0.73}_{-0.70}$	-18.01 ± 0.21
1045	1433	101.9334060	70.1982680	4.5276	1.00	$9.77^{+1.08}_{-1.10}$	$55.0^{+7.0}_{-7.2}$	9.0	$-1.35^{+0.10}_{-0.10}$	-19.24 ± 0.03
1086855	8018	189.2865122	62.2381380	4.4096	1.00	$5.25^{+0.83}_{-0.86}$	$247.3^{+106.5}_{-71.5}$	6.2	$-0.90^{+0.58}_{-0.53}$	-16.97 ± 0.17
10868	5105	268.4410301	65.1676270	4.3886	1.00	$14.65^{+3.26}_{-3.23}$	$125.7^{+44.9}_{-34.6}$	4.5	$-2.67^{+0.49}_{-0.51}$	-18.39 ± 0.12
292585	5224	150.0719633	2.2972652	4.3837	1.00	$7.66^{+0.77}_{-0.71}$	–	10.3	–	–
11024	2767	322.4163338	0.0981286	4.2949	1.00	$61.30^{+6.33}_{-6.44}$	$163.0^{+37.2}_{-30.1}$	9.6	$-2.73^{+0.38}_{-0.39}$	-19.60 ± 0.10
73488	1181	189.1973959	62.1772331	4.1309	1.00	$29.40^{+1.04}_{-1.00}$	$194.2^{+11.2}_{-10.5}$	28.8	$-1.65^{+0.08}_{-0.08}$	-18.77 ± 0.02
4111584	1208	215.9296283	24.1083515	4.0657	1.20	$9.22^{+1.74}_{-1.86}$	$162.7^{+81.5}_{-52.8}$	5.1	$-2.42^{+0.71}_{-0.70}$	-17.47 ± 0.18

[†] The multiply imaged source Abell2744 QSO1

NOTE—Columns: (1) source ID in A. de Graaff et al. (2025a); (2) program ID; (3–4) coordinates; (5) spectroscopic redshift; (6) gravitational magnification factor based on L. J. Furtak et al. (2023b) and G. T. E. Sarrouh et al. (2026), compiled by A. de Graaff et al. (2025a); (7) Lyα flux, the median and 16th/84th percentile uncertainties from the posterior; (8) rest-frame Lyα equivalent width; (9) Lyα signal-to-noise ratio; (10) UV continuum slope; (11) absolute UV magnitude. Sources are sorted by decreasing redshift within each subsample.

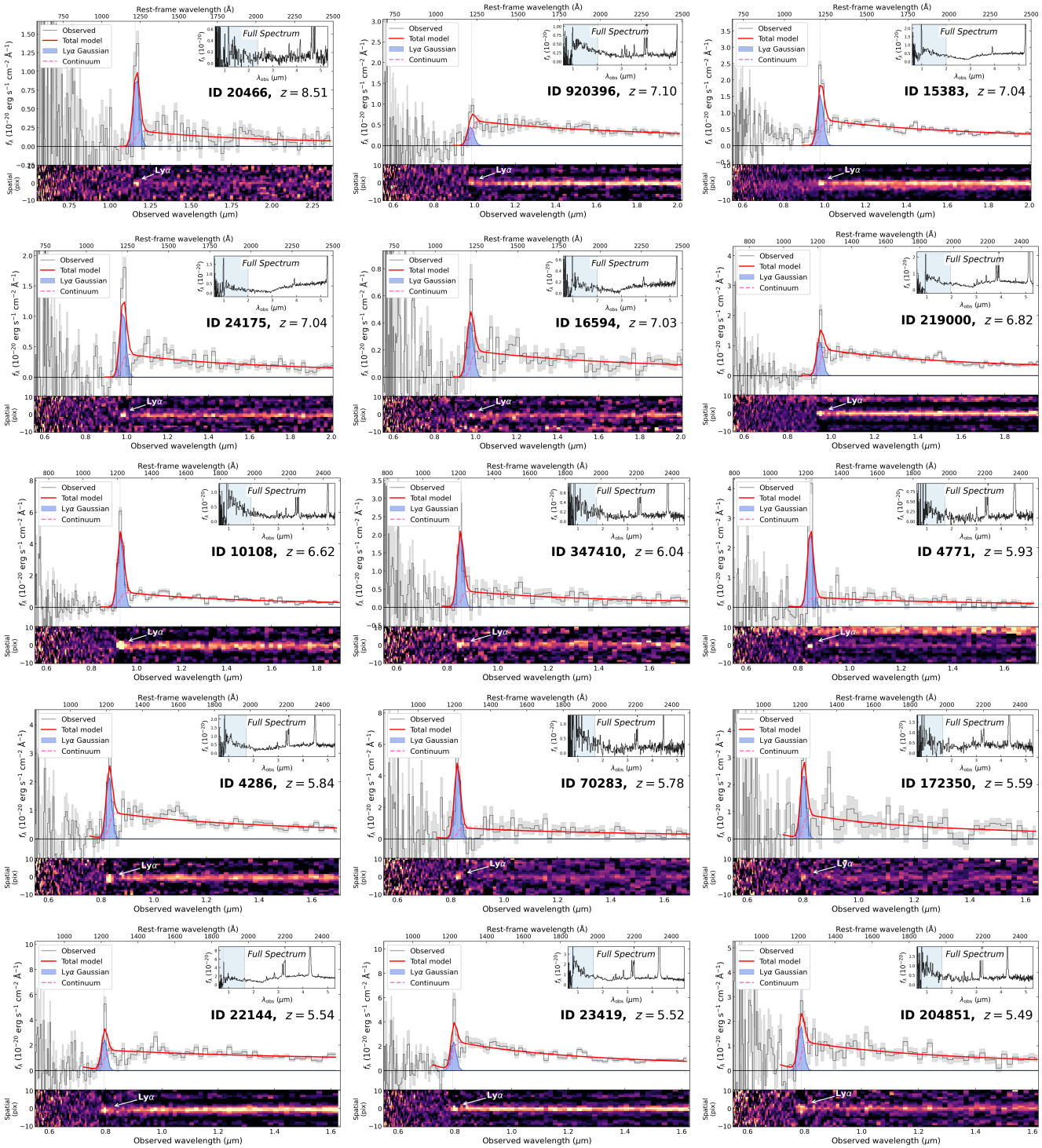

Figure 11. 1D and 2D spectra for LRDs with $z \geq 4$ and Lyα S/N ≥ 3, sorted by decreasing redshift. For each source, the main panel shows the observed 1D spectrum (gray) with the best-fit total model (red), Lyα Gaussian component (blue shaded), and UV continuum (pink dashed). The bottom sub-panel shows the corresponding 2D spectrum. The inset displays the full-wavelength 1D spectrum, with the blue-shaded region marking the wavelength range shown in the main panel.

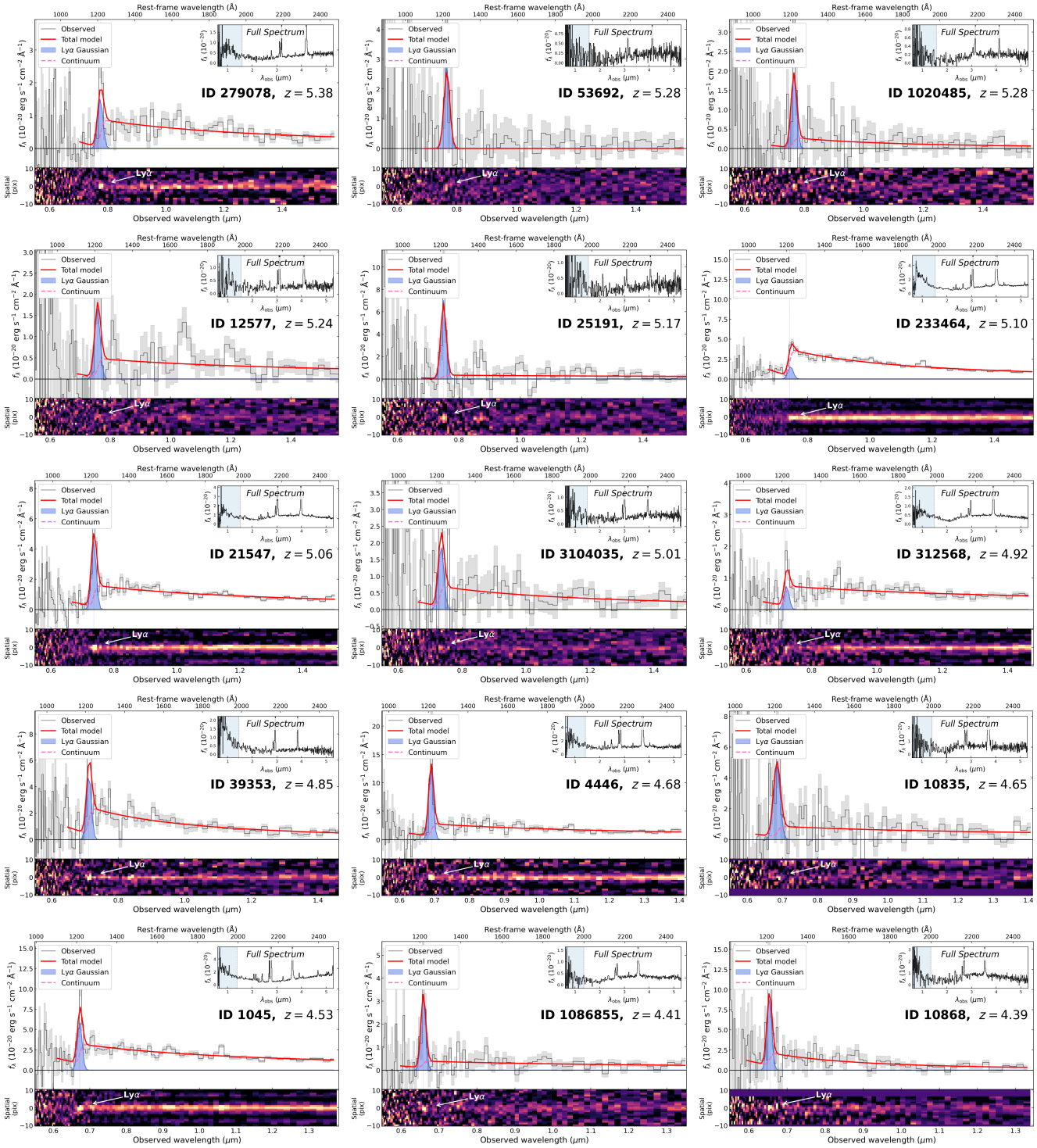

Figure 12. Same as Figure 11, continued.

brightness, indicating a sharper core. This behavior is expected and reflects the advantage of constructing ePSFs from mosaics with finer pixel sampling, when the observational setup permits drizzling onto a finer grid. At a 0.″02 pixel scale, the NIRCam/SW PSF core, with FWHM $\sim$ 0.03–0.06″ depending on wavelength, is sampled by 2–3 pixels across, preserving spatial information that is partially lost when the same data are drizzled to 0.″04 pixels. The finer sampling allows the ePSF construction algorithm to recover a more faithful representation of the intrinsic PSF

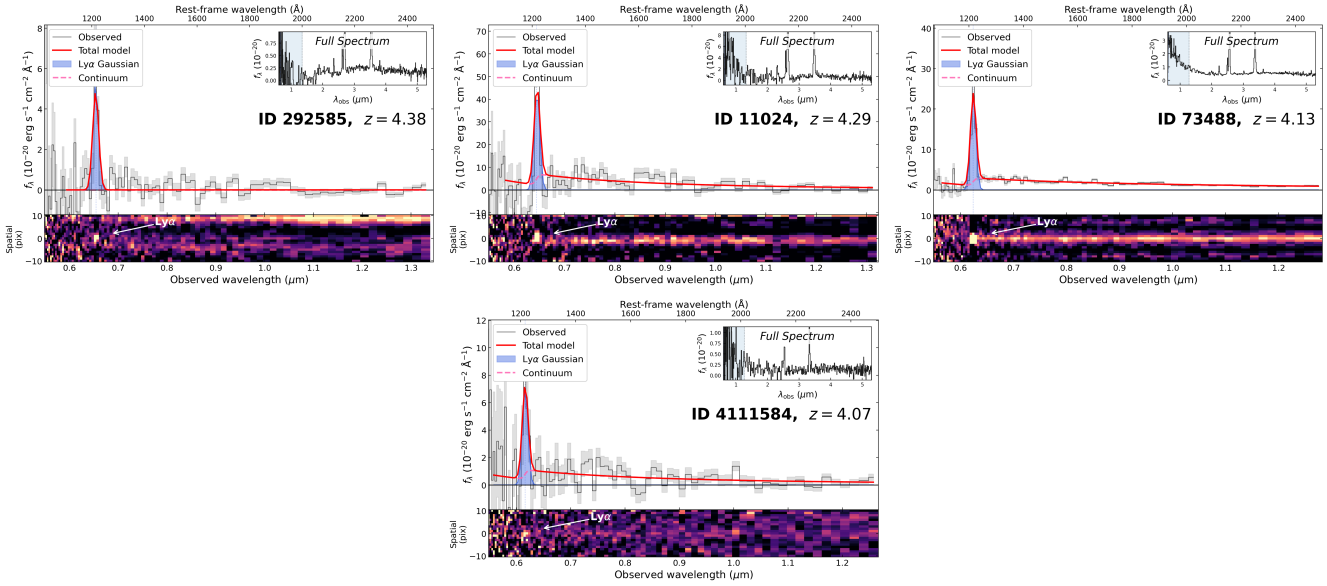

Figure 13. Same as Figure 11, continued.

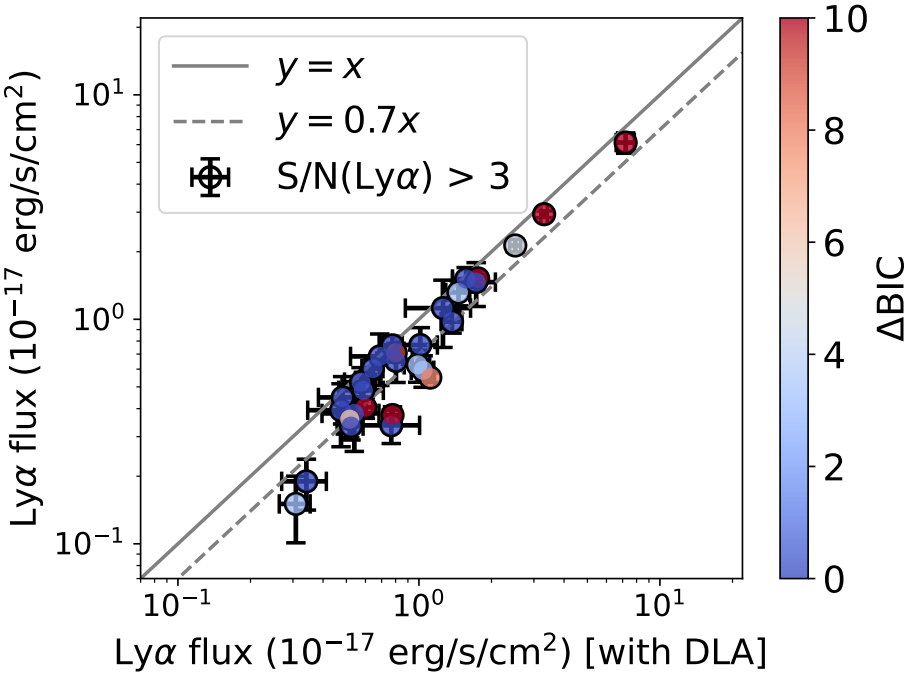

Figure 14. Comparison of the integrated Lyα fluxes measured with the DLA-augmented model against the fiducial (DLA-free, Section 3.1) values for the Lyα-detected LRDs. The solid line marks the 1:1 relation. The two measurements agree at the median level of $\sim 20\%$, comparable to or smaller than the typical measurement uncertainties.

structure, particularly within the innermost resolution element, where the surface-brightness gradient is steepest. At larger radii ($\gtrsim 0.5''$), where the PSF profile varies more slowly and is adequately sampled at either pixel scale, the two ePSFs converge.

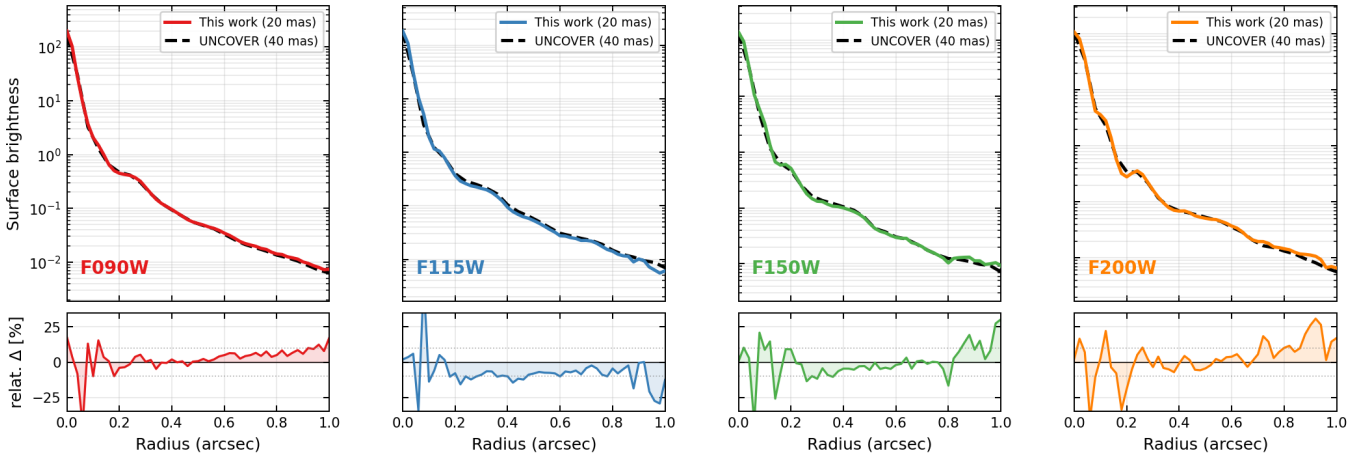

Figure 15. Radial surface brightness profiles of our ePSFs constructed from isolated stars in the A2744 mosaic (solid colored lines) compared with the UNCOVER ePSFs (black dashed lines; J. R. Weaver et al. 2024) for the four NIRCam/SW filters used in this work. Our ePSFs are built at the native 0.″02 pixel scale using the DJA mosaics, while the UNCOVER ePSFs are sampled at 0.″04. Lower panels show the relative difference with respect to the UNCOVER profiles.

D. ASTROMETRIC PRECISION OF THE DJA MOSAICS

Here, we quantify the relative astrometric precision between the F444W and Lyα-filter mosaics in the vicinity of each LRD. In particular, we select bright, compact sources within a 1′ radius of the target LRD by requiring $S/N_{F444W} > 20$ and a half-light radius of < 5 pixels in F444W. For each selected source, we then measure its centroid position in both the F444W and Lyα-filter mosaics using `photutils.centroid`, and finally calculate the median and standard deviation of the astrometric offsets.

Table 3 summarizes the median WCS offset and 1σ scatter for each LRD. The JWST–JWST pairs (LRDs in A2744, CEERS, GOODS, and PRIMER-COSMOS, all using NIRCam filters as the Lyα band) show offsets consistent with zero ($|\Delta\alpha| \lesssim 3$ mas, $|\Delta\delta| \lesssim 2$ mas). The JWST–HST pairs (LRDs in UDS with F814W and GOODS-S with F775W) show slightly larger systematic offsets of 5–11 mas. All of these offsets and standard deviations are $\lesssim$ half a pixel. We thus conclude that the WCS alignment of the DJA mosaics is sufficiently precise for the spatially resolved Lyα analysis presented in the main text.

E. LYα MAPS IN COSMOS AND UDS

Here we present the Lyα maps for five LRDs in COSMOS and UDS (Figure 16), four of which are derived from NIRCam/F090W imaging obtained through the PRIMER program. These F090W images are 2 mag shallower than those in GOODS-S and Abell 2744, resulting in noisier Lyα maps.

F. NIRSPEC/PRISM SPECTRUM OF THE SOUTHERN CLUMP OF LRD 204851

Our Lyα map reveals a remarkable spatial distribution of Lyα emission in LRD 204851 in GOODS-S. The central region of this galaxy is identified as an LRD based on a PRISM spectrum centered on it (second row of Figure 9). The lower, southern clump of this LRD was observed in JWST/DDT program PID 6541 (PI: Egami). As shown in Figure 17, this clump is at the same redshift as the central LRD and exhibits strong Lyα emission, in excellent agreement with our Lyα map. A detailed analysis of this source will be presented in Ji et al. 2026 (in prep.).

REFERENCES

Ananna, T. T., Bogdán, Á., Kovács, O. E., Natarajan, P., & Hickox, R. C. 2024, ApJL, 969, L18, doi: 10.3847/2041-8213/ad5669

Anderson, J., & King, I. R. 2000, PASP, 112, 1360, doi: 10.1086/316632

Ando, M., Harikane, Y., Katz, H., Inayoshi, K., & Tanaka, T. S. 2026, arXiv e-prints, arXiv:2606.03522. https://arxiv.org/abs/2606.03522

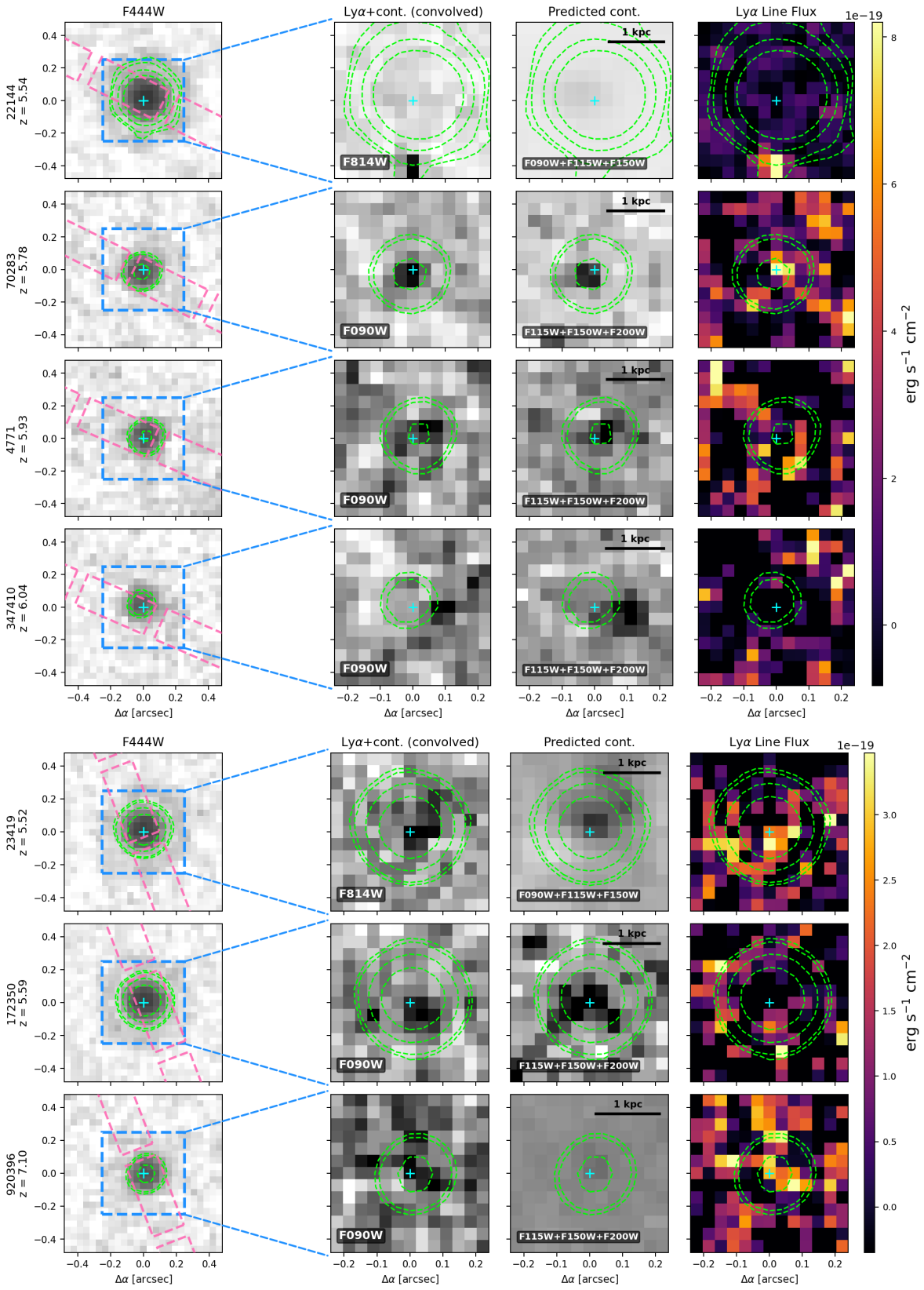

Figure 16. Similar to Figure 8, but for the LRDs in COSMOS (first two rows) and UDS (remaining three rows). We note that the F090W imaging used here is from PRIMER and is relatively shallow, with a 5σ depth of 27.6 AB mag (C. T. Donnan et al. 2024), about 2 magnitudes shallower than JADES and UNCOVER.

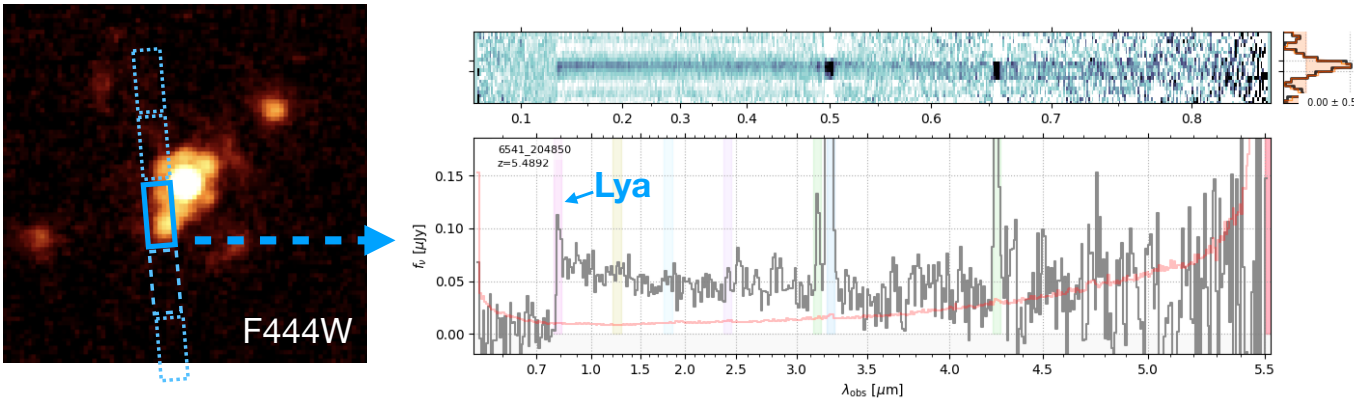

Figure 17. The NIRSpec/PRISM spectrum for the southern clump in LRD 204851 in GOODS-S (second row of Figure 9).

Table 3. WCS Offset Between F444W and Lyα-Filter Mosaics

Field	Source ID	Lyα Filter	Pixel scale[†] (mas)	$\Delta\alpha$ (mas)	$\sigma_{\Delta\alpha}$ (mas)	$\Delta\delta$ (mas)	$\sigma_{\Delta\delta}$ (mas)
A2744	4286	F090W	20	+2.7	13.0	−1.6	9.1
A2744	24175	F090W	20	+1.4	8.1	−0.9	7.0
A2744	20466	F115W	20	+1.4	6.4	+0.6	10.3
COSMOS	22144	HST/F814W	40	−7.0	22.5	+2.2	20.4
COSMOS	4771	F090W	40	+0.3	17.2	−1.2	16.3
COSMOS	347410	F090W	40	+0.2	8.6	−2.2	7.3
COSMOS	70283	F090W	40	−1.7	7.3	+0.6	11.6
EGS	10108	F090W	40	−1.5	8.9	+0.2	9.8
UDS	23419	HST/F814W	40	+5.4	18.0	+6.1	14.2
UDS	172350	F090W	40	+1.0	11.2	−1.2	11.0
UDS	920396	F090W	40	+0.0	11.4	−1.2	10.9
GOODS-S	204851	HST/F775W	40	+10.6	9.7	−6.9	9.6
GOODS-S	219000	F090W	20	−2.9	12.1	+0.5	10.3

[†] Pixel scale of the Lyα map.

NOTE—Median offset ($\Delta\alpha$, $\Delta\delta$) and standard deviation (σ) of the centroid position difference between F444W and the Lyα-filter mosaic, measured from bright compact sources within 1′ of each LRD. Positive $\Delta\alpha$ indicates the F444W centroid is east of the Lyα-filter centroid. Outliers are rejected via iterative 3σ clipping using the MAD.

Asada, Y., Inayoshi, K., Fei, Q., Fujimoto, S., & Willott, C. 2026, arXiv e-prints, arXiv:2601.10573, doi: 10.48550/arXiv.2601.10573
Atek, H., Kunth, D., Hayes, M., Östlin, G., & Mas-Hesse, J. M. 2008, A&A, 488, 491, doi: 10.1051/0004-6361:200809527
Bacon, R., Conseil, S., Mary, D., et al. 2017, A&A, 608, A1, doi: 10.1051/0004-6361/201730833
Bacon, R., Brinchmann, J., Conseil, S., et al. 2023, A&A, 670, A4, doi: 10.1051/0004-6361/202244187
Becker, G. D., Bolton, J. S., Madau, P., et al. 2015, MNRAS, 447, 3402, doi: 10.1093/mnras/stu2646
Begelman, M. C., & Dexter, J. 2026a, ApJ, 996, 48, doi: 10.3847/1538-4357/ae274a
Begelman, M. C., & Dexter, J. 2026b, ApJ, 996, 48, doi: 10.3847/1538-4357/ae274a
Begelman, M. C., Rossi, E. M., & Armitage, P. J. 2008, MNRAS, 387, 1649, doi: 10.1111/j.1365-2966.2008.13344.x
Bezanson, R., Labbe, I., Whitaker, K. E., et al. 2024, ApJ, 974, 92, doi: 10.3847/1538-4357/ad66cf
Bolton, J. S., & Haehnelt, M. G. 2007, MNRAS, 382, 325, doi: 10.1111/j.1365-2966.2007.12372.x
Bosman, S. E. I., Fan, X., Jiang, L., et al. 2018, MNRAS, 479, 1055, doi: 10.1093/mnras/sty1344
Bosman, S. E. I., Davies, F. B., Becker, G. D., et al. 2022, MNRAS, 514, 55, doi: 10.1093/mnras/stac1046
Boucaud, A., Bocchio, M., Abergel, A., et al. 2016, A&A, 596, A63, doi: 10.1051/0004-6361/201629080
Calzetti, D., Armus, L., Bohlin, R. C., et al. 2000, ApJ, 533, 682, doi: 10.1086/308692
Calzetti, D., Kinney, A. L., & Storchi-Bergmann, T. 1994, ApJ, 429, 582, doi: 10.1086/174346
Casey, C. M., Akins, H. B., Finkelstein, S. L., et al. 2025, ApJL, 990, L61, doi: 10.3847/2041-8213/adfa91
Chang, S.-J., Gronke, M., Matthee, J., & Mason, C. 2026, MNRAS, 545, staf2131, doi: 10.1093/mnras/staf2131
Cloonan, A. P., Whitaker, K. E., Manning, S. M., et al. 2026, arXiv e-prints, arXiv:2603.24700, doi: 10.48550/arXiv.2603.24700
de Graaff, A., Hviding, R. E., Naidu, R. P., et al. 2025a, arXiv e-prints, arXiv:2511.21820, doi: 10.48550/arXiv.2511.21820
de Graaff, A., Rix, H.-W., Naidu, R. P., et al. 2025b, A&A, 701, A168, doi: 10.1051/0004-6361/202554681
deGraaff, A., Brammer, G., Weibel, A., et al. 2025, A&A, 697, A189, doi: 10.1051/0004-6361/202452186
Dickinson, M., Amorin, R., Arrabal Haro, P., et al. 2024, The CANDELS-Area Prism Epoch of Reionization Survey (CAPERS),, JWST Proposal. Cycle 3, ID. #6368
Dijkstra, M. 2014, PASA, 31, e040, doi: 10.1017/pasa.2014.33
Donnan, C. T., McLure, R. J., Dunlop, J. S., et al. 2024, MNRAS, 533, 3222, doi: 10.1093/mnras/stae2037
Eilers, A.-C., Davies, F. B., & Hennawi, J. F. 2018, ApJ, 864, 53, doi: 10.3847/1538-4357/aad4fd
Eisenstein, D. J., Willott, C., Alberts, S., et al. 2026, ApJS, 283, 6, doi: 10.3847/1538-4365/ae3163
Fasano, G., & Franceschini, A. 1987, MNRAS, 225, 155, doi: 10.1093/mnras/225.1.155
Finkelstein, S. L., Bagley, M. B., Arrabal Haro, P., et al. 2025, ApJL, 983, L4, doi: 10.3847/2041-8213/adbbd3
Foreman-Mackey, D., Hogg, D. W., Lang, D., & Goodman, J. 2013, PASP, 125, 306, doi: 10.1086/670067
Furtak, L. J., Zitrin, A., Plat, A., et al. 2023a, ApJ, 952, 142, doi: 10.3847/1538-4357/acdc9d
Furtak, L. J., Zitrin, A., Weaver, J. R., et al. 2023b, MNRAS, 523, 4568, doi: 10.1093/mnras/stad1627
Gaia Collaboration, Brown, A. G. A., Vallenari, A., et al. 2021, A&A, 649, A1, doi: 10.1051/0004-6361/202039657
Genin, A., Shuntov, M., Brammer, G., et al. 2025, A&A, 699, A343, doi: 10.1051/0004-6361/202555504
Giavalisco, M., Ferguson, H. C., Koekemoer, A. M., et al. 2004, ApJL, 600, L93, doi: 10.1086/379232
Greene, J. E., Labbe, I., Goulding, A. D., et al. 2024, ApJ, 964, 39, doi: 10.3847/1538-4357/ad1e5f
Greene, J. E., Setton, D. J., Furtak, L. J., et al. 2026, ApJ, 996, 129, doi: 10.3847/1538-4357/ae1836
Grogin, N. A., Kocevski, D. D., Faber, S. M., et al. 2011, ApJS, 197, 35, doi: 10.1088/0067-0049/197/2/35
Gronke, M., Dijkstra, M., McCourt, M., & Oh, S. P. 2017, A&A, 607, A71, doi: 10.1051/0004-6361/201731013
Gunn, J. E., & Peterson, B. A. 1965, ApJ, 142, 1633, doi: 10.1086/148444
Hashemi, S., Becker, G. D., Zhu, Y., & Hong, H. 2025, MNRAS, 542, 104, doi: 10.1093/mnras/staf1225
Hashimoto, T., Garel, T., Guiderdoni, B., et al. 2017, A&A, 608, A10, doi: 10.1051/0004-6361/201731579
Hayes, M. 2015, PASA, 32, e027, doi: 10.1017/pasa.2015.25
Hayes, M., Östlin, G., Mas-Hesse, J. M., et al. 2005, A&A, 438, 71, doi: 10.1051/0004-6361:20052702
Hayes, M., Östlin, G., Schaerer, D., et al. 2013, ApJL, 765, L27, doi: 10.1088/2041-8205/765/2/L27
Heintz, K. E., Brammer, G. B., Watson, D., et al. 2025, A&A, 693, A60, doi: 10.1051/0004-6361/202450243
Herenz, E. C., Urrutia, T., Wisotzki, L., et al. 2017, A&A, 606, A12, doi: 10.1051/0004-6361/201731055
Horne, K. 1986, PASP, 98, 609, doi: 10.1086/131801
Huberty, M., Scarlata, C., Hayes, M. J., & Gazagnes, S. 2025, ApJ, 987, 82, doi: 10.3847/1538-4357/add5e7

Hviding, R. E., de Graaff, A., Miller, T. B., et al. 2025, A&A, 702, A57, doi: 10.1051/0004-6361/202555816
Iani, E., Rinaldi, P., Caputi, K. I., et al. 2025, ApJ, 989, 160, doi: 10.3847/1538-4357/ade5a6
Inami, H., Bacon, R., Brinchmann, J., et al. 2017, A&A, 608, A2, doi: 10.1051/0004-6361/201731195
Inayoshi, K., & Ichikawa, K. 2024, ApJL, 973, L49, doi: 10.3847/2041-8213/ad74e2
Inayoshi, K., & Maiolino, R. 2025, ApJL, 980, L27, doi: 10.3847/2041-8213/adaebd
Inoue, A. K., Shimizu, I., Iwata, I., & Tanaka, M. 2014, MNRAS, 442, 1805, doi: 10.1093/mnras/stu936
Ji, X., Maiolino, R., Übler, H., et al. 2025, MNRAS, 544, 3900, doi: 10.1093/mnras/staf1867
Ji, X., Pezzulli, G., D'Eugenio, F., et al. 2026, arXiv e-prints, arXiv:2604.03370, doi: 10.48550/arXiv.2604.03370
Ji, Z., Alberts, S., Zhu, Y., et al. 2025, ApJL, 988, L69, doi: 10.3847/2041-8213/adf194
Jones, G. C., Bunker, A. J., Saxena, A., et al. 2024, A&A, 683, A238, doi: 10.1051/0004-6361/202347099
Kerutt, J., Wisotzki, L., Verhamme, A., et al. 2022, A&A, 659, A183, doi: 10.1051/0004-6361/202141900
Kido, D., Ioka, K., Hotokezaka, K., Inayoshi, K., & Irwin, C. M. 2025, MNRAS, 544, 3407, doi: 10.1093/mnras/staf1898
Killi, M., Watson, D., Brammer, G., et al. 2024, A&A, 691, A52, doi: 10.1051/0004-6361/202348857
Kocevski, D. D., Finkelstein, S. L., Barro, G., et al. 2025, ApJ, 986, 126, doi: 10.3847/1538-4357/adbc7d
Koekemoer, A. M., Faber, S. M., Ferguson, H. C., et al. 2011, ApJS, 197, 36, doi: 10.1088/0067-0049/197/2/36
Labbé, I., van Dokkum, P., Nelson, E., et al. 2023, Nature, 616, 266, doi: 10.1038/s41586-023-05786-2
Labbe, I., Greene, J. E., Bezanson, R., et al. 2025, ApJ, 978, 92, doi: 10.3847/1538-4357/ad3551
Lambrides, E., Larson, R., Garofali, K., et al. 2024, arXiv e-prints, arXiv:2409.13047, doi: 10.48550/arXiv.2409.13047
Laursen, P., Sommer-Larsen, J., & Andersen, A. C. 2009, ApJ, 704, 1640, doi: 10.1088/0004-637X/704/2/1640
Leclercq, F., Bacon, R., Wisotzki, L., et al. 2017, A&A, 608, A8, doi: 10.1051/0004-6361/201731480
Lin, X., Cai, Z., Wu, Y., et al. 2024, ApJS, 272, 33, doi: 10.3847/1538-4365/ad3e7d
Liu, H., Jiang, Y.-F., Quataert, E., Greene, J. E., & Ma, Y. 2025, ApJ, 994, 113, doi: 10.3847/1538-4357/ae0c19
Ma, Y., Greene, J. E., Setton, D. J., et al. 2025, ApJ, 981, 191, doi: 10.3847/1538-4357/ada613
Madau, P. 1995, ApJ, 441, 18, doi: 10.1086/175332
Madau, P., & Maiolino, R. 2026, arXiv e-prints, arXiv:2602.22386, doi: 10.48550/arXiv.2602.22386
Maseda, M. V., de Graaff, A., Franx, M., et al. 2024, A&A, 689, A73, doi: 10.1051/0004-6361/202449914
Matsuoka, Y., Onoue, M., Iwasawa, K., et al. 2025, ApJ, 988, 57, doi: 10.3847/1538-4357/addf4e
Matthee, J., Naidu, R. P., Brammer, G., et al. 2024, ApJ, 963, 129, doi: 10.3847/1538-4357/ad2345
Naidu, R. P., Matthee, J., Katz, H., et al. 2025, arXiv e-prints, arXiv:2503.16596, doi: 10.48550/arXiv.2503.16596
Naidu, R. P., Oesch, P. A., Brammer, G., et al. 2026, The Open Journal of Astrophysics, 9, 56033, doi: 10.33232/001c.156033
Nikopoulos, G. P., Watson, D., Sneppen, A., et al. 2025, arXiv e-prints, arXiv:2510.06362, doi: 10.48550/arXiv.2510.06362
Oesch, P. A., Brammer, G., Naidu, R. P., et al. 2023, MNRAS, 525, 2864, doi: 10.1093/mnras/stad2411
Ono, Y., Ouchi, M., Mobasher, B., et al. 2012, ApJ, 744, 83, doi: 10.1088/0004-637X/744/2/83
Osterbrock, D. E., & Ferland, G. J. 2006, Astrophysics of gaseous nebulae and active galactic nuclei
Östlin, G., Hayes, M., Kunth, D., et al. 2009, AJ, 138, 923, doi: 10.1088/0004-6256/138/3/923
Pacucci, F., & Narayan, R. 2024, ApJ, 976, 96, doi: 10.3847/1538-4357/ad84f7
Pang, Y., Wang, X., Cheng, C., et al. 2026, arXiv e-prints, arXiv:2602.12548, doi: 10.48550/arXiv.2602.12548
Peacock, J. A. 1983, MNRAS, 202, 615, doi: 10.1093/mnras/202.3.615
Peng, C. Y., Ho, L. C., Impey, C. D., & Rix, H.-W. 2010, AJ, 139, 2097, doi: 10.1088/0004-6256/139/6/2097
Pentericci, L., Vanzella, E., Fontana, A., et al. 2014, ApJ, 793, 113, doi: 10.1088/0004-637X/793/2/113
Pentericci, L., Vanzella, E., Castellano, M., et al. 2018, A&A, 619, A147, doi: 10.1051/0004-6361/201732465
Pérez-González, P. G., Barro, G., Rieke, G. H., et al. 2024, ApJ, 968, 4, doi: 10.3847/1538-4357/ad38bb
Pérez-González, P. G., Barro, G., Carniani, S., et al. 2026, arXiv e-prints, arXiv:2602.20247, doi: 10.48550/arXiv.2602.20247
Planck Collaboration, Aghanim, N., Akrami, Y., et al. 2020, A&A, 641, A6, doi: 10.1051/0004-6361/201833910
Rinaldi, P., Bonaventura, N., Rieke, G. H., et al. 2025, ApJ, 992, 71, doi: 10.3847/1538-4357/adfa10
Rinaldi, P., Hainline, K., D'Eugenio, F., et al. 2026, arXiv e-prints, arXiv:2604.07138, doi: 10.48550/arXiv.2604.07138

Rusakov, V., Watson, D., Nikopoulos, G. P., et al. 2026, Nature, 649, 574, doi: 10.1038/s41586-025-09900-4

Sarrouh, G. T. E., Asada, Y., Martis, N. S., et al. 2026, ApJS, 282, 3, doi: 10.3847/1538-4365/ae1611

Schwarz, G. 1978, Annals of Statistics, 6, 461

Setton, D. J., Greene, J. E., Spilker, J. S., et al. 2025, ApJL, 991, L10, doi: 10.3847/2041-8213/ade78b

Shen, Y., Zhuang, M.-Y., Li, J., et al. 2024, arXiv e-prints, arXiv:2408.12713, doi: 10.48550/arXiv.2408.12713

Sneppen, A., Watson, D., Matthews, J. H., et al. 2026, arXiv e-prints, arXiv:2601.18864, doi: 10.48550/arXiv.2601.18864

Stark, D. P., Ellis, R. S., Chiu, K., Ouchi, M., & Bunker, A. 2010, MNRAS, 408, 1628, doi: 10.1111/j.1365-2966.2010.17227.x

Steidel, C. C., Bogosavljević, M., Shapley, A. E., et al. 2011, ApJ, 736, 160, doi: 10.1088/0004-637X/736/2/160

Storey, P. J., & Zeippen, C. J. 2000, MNRAS, 312, 813, doi: 10.1046/j.1365-8711.2000.03184.x

Sun, W. Q., Naidu, R. P., Matthee, J., et al. 2026, arXiv e-prints, arXiv:2601.20929, doi: 10.48550/arXiv.2601.20929

Tang, M., Stark, D. P., Mason, C. A., et al. 2026, arXiv e-prints, arXiv:2604.03563, doi: 10.48550/arXiv.2604.03563

Taylor, A. J., Finkelstein, S. L., Kocevski, D. D., et al. 2025, ApJ, 986, 165, doi: 10.3847/1538-4357/add15b

Torralba, A., Matthee, J., Pezzulli, G., et al. 2026a, A&A, 707, A75, doi: 10.1051/0004-6361/202557537

Torralba, A., Matthee, J., Pezzulli, G., et al. 2026b, A&A, 705, A147, doi: 10.1051/0004-6361/202555596

Treiber, H., Greene, J. E., Weaver, J. R., et al. 2025, ApJ, 984, 93, doi: 10.3847/1538-4357/adc38f

Urrutia, T., Wisotzki, L., Kerutt, J., et al. 2019, A&A, 624, A141, doi: 10.1051/0004-6361/201834656

Valentino, F., Brammer, G., Gould, K. M. L., et al. 2023, ApJ, 947, 20, doi: 10.3847/1538-4357/acbefa

Vanden Berk, D. E., Richards, G. T., Bauer, A., et al. 2001, AJ, 122, 549, doi: 10.1086/321167

Wang, B., de Graaff, A., Davies, R. L., et al. 2025, ApJ, 984, 121, doi: 10.3847/1538-4357/adc1ca

Weaver, J. R., Cutler, S. E., Pan, R., et al. 2024, ApJS, 270, 7, doi: 10.3847/1538-4365/ad07e0

Williams, C. C., Alberts, S., Ji, Z., et al. 2024, ApJ, 968, 34, doi: 10.3847/1538-4357/ad3f17

Wisotzki, L., Bacon, R., Blaizot, J., et al. 2016, A&A, 587, A98, doi: 10.1051/0004-6361/201527384

Xiao, M., Oesch, P. A., Bing, L., et al. 2025, A&A, 700, A231, doi: 10.1051/0004-6361/202554361

Yang, H., Malhotra, S., Gronke, M., et al. 2017, ApJ, 844, 171, doi: 10.3847/1538-4357/aa7d4d

Yue, M., Eilers, A.-C., Ananna, T. T., et al. 2024, ApJL, 974, L26, doi: 10.3847/2041-8213/ad7eba

Zhang, S., Liu, B., Bromm, V., & Kühnel, F. 2026, ApJL, 1000, L19, doi: 10.3847/2041-8213/ae4bd0

Zheng, Z., Cen, R., Trac, H., & Miralda-Escudé, J. 2010, ApJ, 716, 574, doi: 10.1088/0004-637X/716/1/574

Zhu, Y., Becker, G. D., Bosman, S. E. I., et al. 2021, ApJ, 923, 223, doi: 10.3847/1538-4357/ac26c2